Influence of drift angle on the propulsive efficiency of a fully appended container ship (KCS) using Computational Fluid Dynamics

Yifu Zhang [a,*], Björn Windén [b], Héctor Rubén Díaz Ojeda [c], Dominic Hudson [a], Stephen Turnock [a]

[a] *Maritime Engineering, University of Southampton, Boldrewood Campus, Burgess Road, Southampton, SO16 7QF, Hampshire, UK*
[b] *The Department of Ocean Engineering, Texas A&M University, 727 Ross Street, College Station, 77843, TX, USA*
[c] *Instituto Universitario de Sistemas Inteligentes y Aplicaciones Numéricas en Ingeniería, Universidad de Las Palmas de Gran Canaria (ULPGC), Las Palmas de Gran Canaria, 35017, Spain*

ARTICLE INFO

ABSTRACT

To estimate the powering and manoeuvring performance of the ship in a real seaway, it is essential to accurately determine forces acting on the hull, propeller, rudder and their interaction effects when operating at an angle of drift. The rotating propeller alters the fluid flow around the upstream hull and the downstream rudder. Likewise, when a non-zero drift or rudder angle is applied, significant crossflow is generated across the propeller plane, changing the wakefield and the actual performance of the propeller. A study is conducted to analyse the hull–propeller–rudder interaction of the benchmark KRISO Container Ship (KCS) in calm water using Computational Fluid Dynamics (CFD). The KCS is studied at drift angles of −10°, 0° and +10°, combined with a series of rudder angles (−35° to +35°), which can represent quasi-static phases of an actual ship manoeuvre. The propeller is modelled using two body force models, Blade Element Momentum Theory and the Yamazaki model. Good agreement is found between experimental and numerical results when predicting hull forces and wave patterns at drift, providing a good reference for experimental measurement of the hull and its appendage forces at drift and future validation of actual dynamic manoeuvring simulations.

1. Introduction

Accurate prediction of ship manoeuvring and coursekeeping in a seaway is one of the essential requirements in ship design. It is closely related to ship navigation safety, especially in adverse wave and wind conditions. The International Maritime Organization (IMO) (International Maritime Organization, 2002) released ship manoeuvrability standards, emphasizing the necessity of checking ship manoeuvring during the early ship design stage. Although ship manoeuvring calculations in calm water have been studied widely, the understanding of ship manoeuvrability in real sea states is still not well established (ITTC, 2021). Compared to resistance, propulsion, and seakeeping, the ability to anticipate how a ship will manoeuvre in waves remains a significant challenge because of the complex fluid–structure interaction between hull, rudder, propeller and fluid (Sanada et al., 2021). Free-running model testing and captive model tests in a towing tank or wave basin are two standard experimental methods for assessing a ship's manoeuvrability. Manoeuvrability is evaluated in a straightforward manner during free-running model testing by performing a prescribed turning or zigzag test. Captive tests, on the other hand, are used to estimate hydrodynamic forces and moments by solving ship motion equations using the derived hydrodynamic derivatives (manoeuvring coefficients) (Jiang et al., 2022). Although relatively accurate and reliable manoeuvring assessments can be obtained by the conventional model test, it is still costly and has a high specification for the ship model and test facilities. The rapid advancement of high performance computing has allowed numerical methods to provide a potentially more cost-effective method of determining the ship's manoeuvring performance, with greater fidelity of hull-appendage interaction in the stern region, which is less likely to be captured in towing tank tests.

When determining the characteristics of a ship's manoeuvring and powering in real sea states, it is important to acquire accurate estimates of the forces and moments acting on both the hull and its appendages. This is especially true when the ship is operating at the angle of drift, as the influence of rudder angle and drift angle could be significant in assessing the ship resistance, propulsion coefficients, and overall efficiency of the propulsion system. The effective rudder angle is one of the main criteria that determines how the hull and rudder forces

behave (Molland and Turnock, 2002). When a non-zero rudder angle is applied to alter the ship's course, the ship develops a yaw or drift angle and the flow is no longer aligned with the vessel, and a crossflow is formed across the propeller plane. Therefore, the actual propeller performance, such as thrust, torque and effective direction of the propeller race, will be changed due to the asymmetry flow. The propeller sideforce will not keep constant as that in straight-head conditions, leading to a decrease in the effective inflow angle to the rudder (Badoe et al., 2015). Additionally, the effective inflow angle to the rudder is recovered or increased due to the existence of the hull and propeller upstream of the rudder, which straightens the flow. Therefore, the flow straightening effect due to the hull and propeller is important in the precise determination of rudder forces during a ship manoeuvre. Drift angle and flow straightening effects have been investigated using experimental and numerical methods. Molland and Turnock (1995) used wind tunnel tests to examine the flow straightening influence of the propeller on the effective drift angle and how it affects the rudder performance. Longo and Stern (2002) investigated the effect of drift angle on forces and moments of Series 60 $C_B = 0.6$ cargo/container model ship through towing tank tests. El Moctar (2001) calculated the hull forces as a function of drift angle by applying a finite volume method to viscous flow computations. Phillips et al. (2009) coupled a Reynolds averaged Navier Stokes (RANS) solver with Blade Element Momentum Theory (BEMt) to study self-propelled KVLCC2 hull's manoeuvring coefficients at drift conditions. Badoe et al. (2015) investigated how the angle of drift and the varying length of an upstream body affect the resolution of flow straightening effects. More recently, Sanada et al. (2021) combined experiments and CFD to explore the physics of KCS hull-appendages interaction for turning circles and the reason for differences between port and starboard turning. Sumislawski et al. (2022) examined the JBC hull and propeller interaction under static positive and negative drift conditions, and detailed properties of the fore-body vortex were presented. However, few works have been conducted on the influence of both drift angles and rudder angles on the forces exerted upon the hull, the propeller, the rudder, and their hydrodynamic interaction. Besides, due to the growing demand for newly built ships meeting IMO standards, the use of wind-assist devices for ship propulsion is likely to be used more often as one of the efficient and eco-friendly options. Compared to conventional ships, wind-assisted vessels typically operate at an angle of drift and use the rudder to compensate for the large side forces and yaw moments they experience. Therefore, a good understanding of the effects of drift angle combined with rudder angles on ship powering is essential not only in the assessment of ship coursekeeping and manoeuvring abilities but also in providing a reference for future wind-assisted vessels' design and operation.

In this paper, the hull–propeller–rudder interaction of the benchmark KRISO Container Ship (KCS) in calm water is studied using Computational Fluid Dynamics (CFD). The fully appended KCS is simulated at static drift angles combined with a series of rudder angles, which represent quasi-static phases of an actual ship manoeuvre. This approach removes the need for modelling the complete time varying manoeuvre. It greatly reduces the computational cost and provides sound knowledge for experimental measurements of hull and appendage forces when the angle of drift or non-zero rudder angle is applied.

The numerical methodology used in this study is presented in Section 2, briefly describing governing equations, URANS solver and body force propeller modelling. Then, a case description is shown in Section 3, where an introduction to the hull geometry, coordinate systems for drift computations, and details of computational simulations are made. Section 4 includes the process of grid generation and numerical validation. Then, the numerical results obtained are presented in Section 5 and a comparison is made with experimental data from tests in the Boldrewood Towing Tank. Finally, conclusions drawn from this study are given in Section 6.

2. Numerical methodology

2.1. Governing equations

The motion of the fluid around the fully appended KCS in drift conditions can be modelled using the unsteady Reynolds Averaged Navier–Stokes (RANS) equations. With the assumption of an incompressible fluid, the set of equations can be expressed in the form:

$$\frac{\partial \overline{u}_i}{\partial x_i} = 0 \tag{1}$$

$$\rho \frac{\partial \overline{u}_i}{\partial t} + \rho \frac{\partial \overline{u}_i \overline{u}_j}{\partial x_j} = -\frac{\partial \overline{p}}{\partial x_i} + \frac{\partial}{\partial x_j}\left[\mu\left(\frac{\partial \overline{u}_i}{\partial x_j} + \frac{\partial \overline{u}_j}{\partial x_i}\right)\right] - \rho \frac{\partial \overline{u'_i u'_j}}{\partial x_j} + \overline{F}_i \tag{2}$$

where $\overline{\mathbf{u}}$ and $\overline{p}$ are the mean velocity and pressure fields, ρ is the fluid density, and μ is the dynamic viscosity. The Reynolds stress $\overline{u'_i u'_j}$ is modelled using the Shear Stress Transport (SST) $k - \omega$ turbulence model to achieve turbulence closure. This model was initially developed by Menter (1994), including a blending function that smoothly transitions between the $k - \omega$ and k-ϵ models. The SST $k - \omega$ model has been successfully adopted for analysing hull–propeller–rudder interaction (Larsson et al., 2013) and computing manoeuvring hydrodynamic forces in drift motion (Phillips et al., 2009; Qiu et al., 2010).

2.2. Unsteady RANS solver

The governing equations are numerically solved using the open-source RANS solver OpenFOAM version 7 (OpenFOAMFoundation, 2019). The unsteady RANS equations are discretized using the Finite Volume Method (FVM). In the discretization process, an Euler scheme is employed for temporal discretization and a second-order upwind scheme is utilized for the convection term. The gradient discretization is achieved using the Gauss linear scheme and the Laplacian scheme is discretized using the Gauss linear corrected approach. The interFoam solver in OpenFOAM, which is specifically designed for simulating two-phase flows and calculating the interactions between two immiscible, incompressible fluids such as water and air, is adopted. The pressure velocity coupling is achieved using the PIMPLE algorithm, which is a combination of PISO and SIMPLE. The PIMPLE includes both velocity correction and under relaxation, making PIMPLE more suitable for transient flow modelling, especially for ship stern flows where unsteady fluid effects are prominent.

The Volume of Fluid (VOF) method is used to capture the effect of free surface and to represent the dynamic behaviours of the interface between water and air. The VOF method is based on the equation where the volume fraction α is governed by:

$$\frac{\partial \alpha}{\partial t} + \nabla \cdot (\alpha \mathbf{u}) = 0 \tag{3}$$

where α represents the volume fraction of one phase in a two-phase flow, and $\mathbf{u}$ is the velocity vector of the flow. A cell with a volume fraction value of $\alpha = 1$ represents a cell that is completely filled with water, while a value of $\alpha = 0$ indicates a cell that is completely filled with air. Therefore, the interface between the two phases, or the free surface, is formed by the cells that have intermediate values of α, with $0 < \alpha < 1$. These cells contain a mixture of water and air, and the distribution of α values across the cells is used to track the location and shape of the free surface accurately. The local density ρ and viscosity μ can be determined by the following equations based on the corresponding α value:

$$\rho = \alpha \rho_{water} + (1 - \alpha)\rho_{air} \tag{4}$$

$$\mu = \alpha \mu_{water} + (1 - \alpha)\mu_{air} \tag{5}$$

2.3. Propeller modelling

In the current study, the simulations primarily concern the interaction effects among the hull, propeller, and rudder under drift conditions, rather than directly focusing on the propeller itself. Therefore, two body force models are employed for propeller analysis in this work, namely Blade Element Momentum Theory (BEMt) and the Yamazaki model. In contrast to fully discretized propellers, body force models eliminate the requirement for generating a rotating sub-domain or mesh with complicated propeller blade resolution. This approach not only reduces computational expenses but also mitigates geometric complexities, particularly for propellers operating near, or even within, stationary flow. In body force methods, the momentum generated by rotating propeller blades can be directly added to the RANS momentum equation as an extra momentum source or body force. The RANS momentum equations, when articulated in Cartesian coordinates, show that the flow field, denoted by $\overline{u} = (u, v, w)$, is accelerated by the body force symbolized as $\overline{F_v} = (F_{vx}, F_{vy}, F_{vz})$. Consequently, the momentum equations incorporating the body force term can be represented as follows:

$$\frac{\partial(\rho u)}{\partial t} + \nabla \cdot (\rho u \overline{u}) = -\frac{\partial p}{\partial x} + \frac{\partial \tau_{xx}}{\partial x} + \frac{\partial \tau_{yx}}{\partial y} + \frac{\partial \tau_{zx}}{\partial z} + \rho F_{vx}$$

$$\frac{\partial(\rho v)}{\partial t} + \nabla \cdot (\rho v \overline{u}) = -\frac{\partial p}{\partial y} + \frac{\partial \tau_{xy}}{\partial x} + \frac{\partial \tau_{yy}}{\partial y} + \frac{\partial \tau_{zy}}{\partial z} + \rho F_{vy} \quad (6)$$

$$\frac{\partial(\rho w)}{\partial t} + \nabla \cdot (\rho w \overline{u}) = -\frac{\partial p}{\partial z} + \frac{\partial \tau_{xz}}{\partial x} + \frac{\partial \tau_{yz}}{\partial y} + \frac{\partial \tau_{zz}}{\partial z} + \rho F_{vz}$$

2.3.1. Yamazaki model

A description of the Yamazaki model is made here based on Windén (2021a) and Windén (2021b). It was originally developed by Yamazaki (1968) and improved on by Moriyama (1979) and Yamazaki (1998). It depicts the propeller's interaction with the fluid by distributing bound vortices with a strength of Γ as a substitute for the propeller blades, and a free vortex with a pitch of h to symbolize the trailing wake. The strength $\Gamma(r, \theta)$ is discretely distributed over a concentric grid $[r, \theta]$ that is centred around the propeller's centre of mass. This forms a combined theory that integrates elements from both lifting line and lifting surface theories.

• The calculation of propeller flow

$\Gamma(r, \theta)$ and $h(r)$ are determined iteratively by blending 2D airfoil theory, potential flow, propeller inflow, and the interaction between the free vortex and the blades at the propeller's plane. The propeller-induced velocity disturbance is represented by the velocity potential $\varphi_{Pf\infty}$, which is derived from the Green's function G_P. This Green's function captures the cumulative effect of $\Gamma(r', \theta')$ from every grid-panel on the overall disturbance at $[r, \theta]$. In this context, r_0 represents the propeller's radius while r_h signifies the hub's radius.

$$\varphi_{Pf\infty} = \frac{1}{4\pi} \int_{r_h}^{r_0} r' dr' \int_0^{2\pi} \Gamma(r', \theta') G_p d\theta' \quad (7)$$

$$G_p = \frac{r'}{h(r') R_{20}} - \frac{r \sin(\theta' - \theta)}{r'^2 + r^2 - 2rr' \cos(\theta' - \theta)} \left(1 + \frac{x}{R_{20}}\right) \quad (8)$$

The disturbance is inversely proportional to the distance R_{20} from the source where

$$R_{20} = \sqrt{x^2 + r'^2 + r^2 - 2r'r \cos(\theta' - \theta)} \quad (9)$$

Given the disturbed velocity, the wake velocity, the propeller geometry, the strength of bound vortices, and the pitch of the free vortex, the boundary condition for the propeller, which defines the velocity at its blades, can be established as:

$$\left(\frac{2\sqrt{r^2 + a(r)^2}}{Z k_1 c(r)} + \frac{r^2 + h(r)^2}{2rh(r)\kappa_N(r)}\right) \Gamma(r, \theta) + \left[\frac{\partial \phi_{Pf\infty}}{\partial x_p}\right]_P - \frac{h(r)}{r} \left[\frac{\partial \phi_{Pf\infty}}{\partial \theta}\right]_P$$

$$= \frac{a(r)}{r} \left(\Omega r + [u_{p\theta}(r, \theta)]_P\right) - [u_{px}(r, \theta)]_P \quad (10)$$

Where $a(r)$ and $c(r)$ describe the blade pitch and chord distributions. Z is the number of propeller blades and Ω is rotation rate of propeller. The index $[]_P$ indicates values on propeller disk ($x = 0$) and $u_{px}(r, \theta)$, $u_{p\theta}(r, \theta)$ are the undisturbed axial and tangential velocity distributions in the nominal wake. $\kappa_N(r)$ is the Prandtl tip correction factor and k_1 is an empirical correction for lift slope by Yamazaki (1968), defined as:

$$\kappa_N(r) = \frac{2}{\pi} \cos^{-1}\left(e^{-Z\left(1 - \frac{r}{r_0}\right)\frac{\sqrt{r^2 + h(r)^2}}{h(r_0)}}\right)$$

$$k_1 = \left[1.07 - 1.05 \frac{c(r)}{r_0} + 0.375 \left(\frac{c(r)}{r_0}\right)^2\right]_{r = 0.7 r_0} \quad (11)$$

The undisturbed velocities, $u_{px}(r, \theta)$ and $u_{p\theta}(r, \theta)$, necessitate a clear understanding of the propeller's total induced velocities for effective coupling with a RANS solver. By subtracting these from the velocities presented on the propeller plane by RANS, the undisturbed wake can be identified. Additionally, these total velocities aid in calculating the momentum transferred to the fluid, which subsequently helps determine the thrust and torque. The induced velocities in both axial and tangential directions are described as:

$$V_{Px} = \frac{r\Gamma(r, \theta)}{2h(r)\kappa_N(r)} + \left[\frac{\partial \varphi_{\infty}}{\partial x}\right]_P \qquad \overline{V_{Px}} = \int_0^{2\pi} V_{Px} d\theta \quad (12)$$

$$V_{P\theta} = -\frac{\Gamma(r, \theta)}{2\kappa_N(r)} + \left[\frac{\partial \varphi_{\infty}}{r\partial \theta}\right]_P \qquad \overline{V_{P\theta}} = \int_0^{2\pi} V_{P\theta} d\theta \quad (13)$$

The definition specifies that both the induced velocity in the radial direction and the radial force are zero. Using these velocities, the pitch of the free vortex can be determined as:

$$h(r) = k_2 r \frac{\overline{V_{Px}}}{\overline{V_{P\theta}}} \qquad k_2 = 1 + 0.625 \left(\frac{c_{max} - 0.84}{r_0}\right) \quad (14)$$

Eqs. (7)–(14) are solved iteratively until convergence of h is found.

• The calculation of forces

By integrating the pressure and viscous force components deriving from the vortex strength and the induced momentum, the total thrust T and total torque Q can be calculated:

$$T = -F_{Px} = -\rho \int_{r_h}^{r_0} dr \int_0^{2\pi} \frac{d^2 F_{px}}{dr d\theta} r d\theta + \frac{dF_{fx}}{dr} \quad (15)$$

$$Q = M_{Px} = \rho \int_{r_h}^{r_0} r dr \int_0^{2\pi} \frac{d^2 F_{p\theta}}{dr d\theta} r d\theta + \frac{dF_{f\theta}}{dr} \quad (16)$$

The pressure force components are defined as:

$$\frac{d^2 F_{Px}}{dr d\theta} = \Gamma(r, \theta) V_{P\theta} \qquad \frac{d^2 F_{P\theta}}{dr d\theta} = \Gamma(r, \theta) V_{Px} \quad (17)$$

The viscous force components are defined as:

$$\frac{dF_{Px}}{dr} = -\frac{1}{2} C_{PD} Z c(r) \sqrt{1 + \frac{h(r)^2}{r^2}} \overline{V_{Px}} \overline{V_{P\theta}}$$

$$\frac{dF_{P\theta}}{dr} = -\frac{1}{2} C_{PD} Z c(r) \sqrt{1 + \frac{h(r)^2}{r^2}} \overline{V_{P\theta}}^2 \quad (18)$$

By applying the forces determined from Eqs. (17) and (18) as momentum sources in the RANS simulation via Equation (6), and employing the thrust and torque derived from Eqs. (15) and (16) to control the rotation rate, the Yamazaki model is established that can predict the performance of a certain hull/propeller combination.
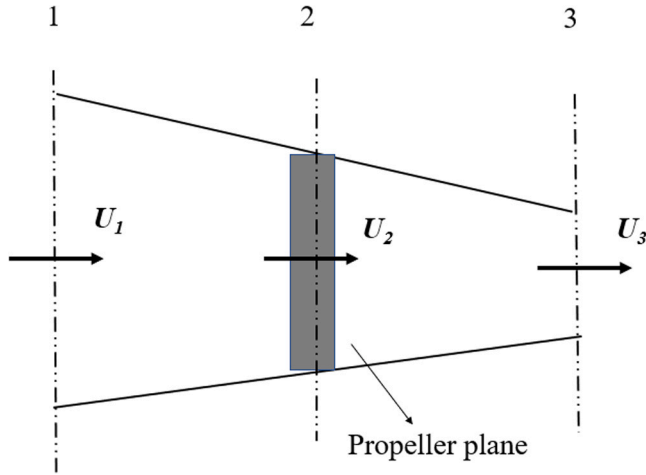
Fig. 1. Momentum representations of propeller plane.

2.3.2. Blade Element Momentum Theory (BEMt)

The Blade Element Momentum theory (BEMt), initially proposed by Burrill (1944), integrates the two-dimensional blade element theory with momentum changes derived from momentum theory. This integration enables the calculation of the effective angle of attack for each section, leading to the determination of the respective thrust and torque contributions of each section. The implementation of BEMt employed in this study adheres to the methodology outlined by Molland et al. (2017), but it is described briefly for better readability. The distance from the centreline is normalized using the propeller radius R, such that the local radius r can be expressed as $r = xR$, where x represents the dimensionless radius.

• Momentum theory

As shown in Fig. 1, Considering the fluid flow within an annular region of radius r and thickness dr in the stream tube, the mass flow rate traversing the respective section at the propeller plane can be described as $\dot{m} = 2\pi r dr \rho U_2$. Velocities at planes 2 and 3, U_2 and U_3, can be expressed with far upstream velocity and the axial inflow factors: $U_2 = U_1(1 + a)$ and $U_3 = U_1(1 + 2a)$. Therefore, the thrust and torque generated by the propeller can be written as:

$$dT = 4\pi r \rho U_1^2 Ka(1+a)dr \qquad dQ = 4\pi r^3 \rho U_1 \Omega Ka'(1+a)dr \qquad (19)$$

Where a is the axial inflow factor, K is the Goldstein factor to account for the propeller with a finite number of blades (Goldstein, 1929), Ω is the angular velocity of the propeller, a' is the circumferential inflow factor. The local efficiency η can be found:

$$\eta = \frac{U_1 \frac{dT}{dr}}{\Omega \frac{dQ}{dr}} = \left(\frac{U_1}{r\Omega}\right)^2 \frac{a}{a'} \qquad (20)$$

Non-dimensionalizing Equation (19) in terms of K_T, K_Q and J:

$$dK_T = \pi x J^2 Ka(1+a)dx \qquad dK_Q = \frac{1}{2}\pi x^3 JKa'(1+a)dx \qquad (21)$$

• Blade element theory

As shown in Fig. 2(a), the lift dL and drag dD for a element with span dr can be written as:

$$dL = \frac{1}{2}\rho Z c(r) U_{\text{foil}}^2 C_L(\alpha)dr \qquad dD = \frac{1}{2}\rho Z c(r) U_{\text{foil}}^2 C_D(\alpha)dr \qquad (22)$$

Where Z is the number of blades, $c(r)$ is the local chord of the blade. The drag and lift coefficients C_D and C_L depend on the angle of attack

α and are determined from experimental tests. The thrust and torque shown in Fig. 2(b) can be derived from lift and drag:

$$dT = dL \cos\phi(1 - \tan\phi \tan\gamma) \qquad dQ = r dL \cos\phi(\tan\phi + \tan\gamma) \qquad (23)$$

Combining Eq. (23), the local efficiency can be written as:

$$\eta = \frac{\tan\psi}{\tan(\phi + \gamma)} \qquad \tan\gamma = \frac{dD}{dL} \qquad (24)$$

Where ψ is the undisturbed flow angle, ϕ is the hydrodynamic pitch angle, γ is defined in Eq. (24), as shown in Fig. 2(a)

• Coupling of Blade element and momentum theories

The coupling is achieved using two independent expressions for local efficiency, which allows the axial and circumferential inflow factors to be expressed as:

$$a' = 1 - \eta_i(1 + a) \qquad a = \frac{1 - \eta_i}{\eta_i + \frac{1}{\eta}\tan^2\psi} \qquad (25)$$

Finally, an iterative method is applied to determine the angle of attack and consequently the inflow factors a and a'. This is done by first assuming a value for α and assuming C_D to be 0, leading to γ being 0 and η being equal to η_i. The coupling of RANS and BEMt has been demonstrated in predicting ship hydrodynamic performance and hull–propeller–rudder interaction (Windén, 2014; Badoe, 2015; Zhang et al., 2021). Furthermore, BEMt has proven to be an accurate and cost-efficient approach for predicting RANS calculations of static drift and manoeuvring performance of self-propelled ships (Turnock et al., 2008; Zhang et al., 2022).

In summary, both the BEMt and Yamazaki models include both axial and circumferential body forces. The integral values of these correspond to the stated thrust and torque values respectively. However, the BEMt lacks the capacity to properly account for tangential inflow velocities compared to the Yamazaki model.

3. Case description

3.1. Hull geometry

In this study, the KCS is selected as the subject vessel, given extensive previous research in both experimental and computational investigations. As a contemporary container ship, the KCS offers comprehensive insights into fluid dynamics and serves as an exemplary model for validating and verifying numerical calculations in ocean engineering applications. The KCS's body plan and profiles are illustrated in Figs. 3 and 4. Table 1 presents the main particulars of KCS, and the model of scale ratio λ=31.60 (L_{PP} = 7.2786 m) is used in this study for all numerical computations, corresponding to KCS model 1 of the 2015 Tokyo CFD workshop (Hino et al., 2020).

3.2. Coordinate systems for drift computations

The simulation of a ship operating under drift conditions necessitates the consideration of two different coordinate systems, as the ship's longitudinal and transverse axes deviate from alignment with those of the computational domain. Consequently, two coordinate systems are employed in this study incorporating both the computational domain system and the ship-fixed system. Adhering to the right-hand rule, these coordinate systems are illustrated in Fig. 5. In this study, the majority of hydrodynamic forces and moments calculations are based on the ship-fixed coordinate system O-XYZ unless otherwise stated. This system features an x-axis directed towards the bow, a y-axis pointing towards the starboard, and an origin situated at the mid-ship. β is the angle of drift of the ship, β_r represents the rudder angle relative to the ship axis. The drift angle, β, is defined as positive when the ship deviates towards the starboard side. The rudder angle β_r is defined as positive when the rudder is turned to the starboard (right when facing forward).
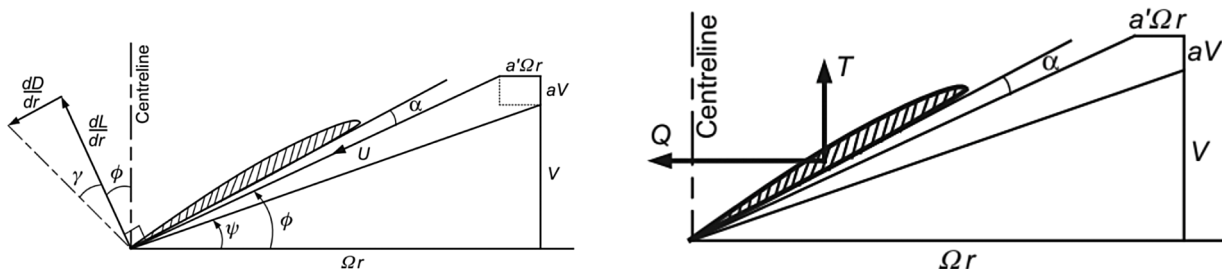
(a) Blade element diagram (Molland et al., 2017)   (b) Blade element representations of propeller action (Molland et al., 2017)
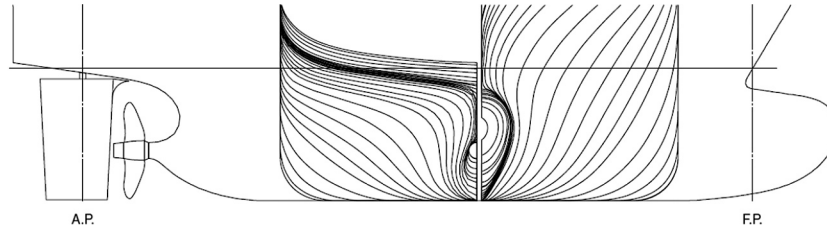
Fig. 2. Blade element theory.

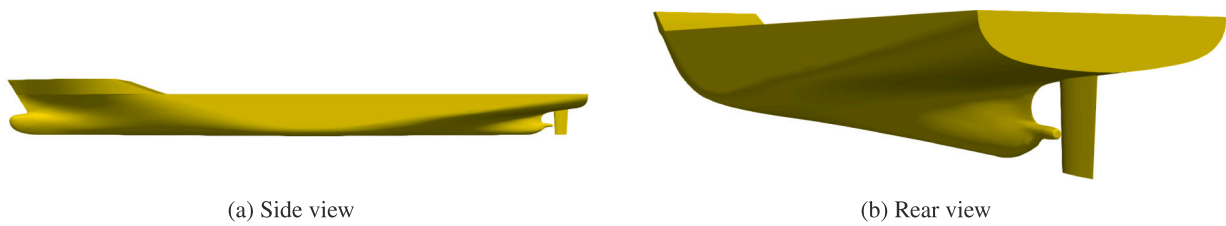**Fig. 3.** Body plan and profile elevation of KCS.

(a) Side view   (b) Rear view

Fig. 4. The geometry of the KCS hull (Hino et al., 2020).

Table 1
Main particulars of KCS.

Parameter	Full scale	Tokyo'15 model 1 scale	SOTON model scale
Scale ratio, λ	1	31.60	60.96
Length between perpendicular, L_{pp}	230 m	7.2786 m	3.7729 m
Maximum beam of waterline, B_{WL}	32.2 m	1.0190 m	0.53 m
Depth, D	19 m	0.6013 m	0.282 m
Draft, T	10.8 m	0.3418 m	0.1772 m
Displacement, ∇	52030 m^3	1.6490 m^3	0.2297 m^3
Wetted surface area w/o rudder, S_W	9424 m^2	9.4379 m^2	2.5359 m^2
Froude Number, Fn	0.26	0.26	0.26
Design speed, U	12.35 m/s	2.196 m/s	1.5818 m/s
Propeller diameter, D_P	7.9 m	0.25 m	0.13 m
Propeller hub ratio, D_H/D_P	0.18	0.18	0.18
The number of propeller blades, Z	5	5	5
Propeller rotation direction (view from stern)	clockwise	clockwise	clockwise

As depicted in Fig. 5, the ship's resistance is denoted by R, while F_Y represents the lateral force exerted on the hull and M_Z signifies the yaw moment. Regarding the rudder force, D corresponds to the rudder drag, and L refers to the rudder lift. These parameters are evaluated within the ship's coordinate system.

3.3. Computational simulations

3.3.1. Simulation conditions

Three sets of simulations are carried out on the KCS hull with the rudder. Three different angles of drift are chosen: $\beta = -10°$, $\beta = 0°$, $\beta = +10°$. For each drift case, a series of static rudder angles are applied. The calm water resistance test is conducted for all cases initially. Subsequently, five sets of fixed RPM tests are performed with

RPM values = 600, 720, 900, 1200, and 1500. The specifics of the simulation conditions are presented in detail below.

- KCS at drift angle, $\beta = 0°$, with eleven static rudder angles, $\beta_r = -35°, -30°, -20°, -10°, -5°, 0°, 5°, 10°, 20°, 30°, 35°$.
- KCS at drift angle, $\beta = -10°$, with seven static rudder angles, $\beta_r = -20°, -10°, -5°, 0°, 5°, 10°, 20°$.
- KCS at drift angle, $\beta = +10°$, with seven static rudder angles, $\beta_r = -20°, -10°, -5°, 0°, 5°, 10°, 20°$.

3.3.2. Computational domain and boundary conditions

The computational domain for numerically simulating the KCS hull with a rudder is established according to the CFD application guidelines set forth by the ITTC (ITTC, 2014). The inlet boundary is situated at 1.0

Table 2
The selected boundary conditions for VOF simulations.

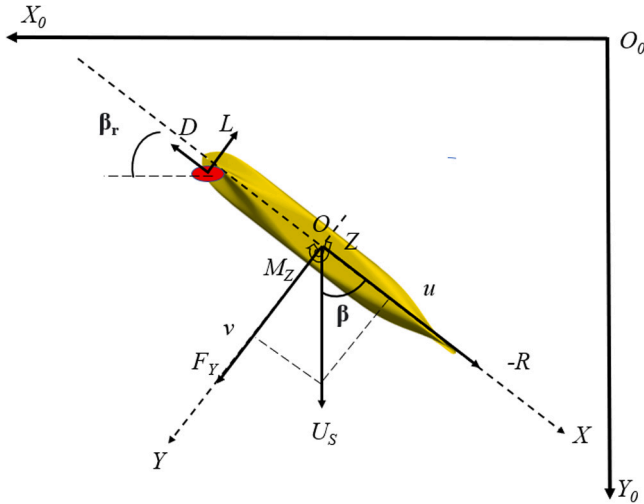| Parameter	Inlet	Outlet	Top	Sides/Bottom	Hull/Rudder
U	fixedValue	inletOutlet	pressureInletOutletVelocity	Symmetry	movingWallVelocity
p	fixedFluxPressure	zeroGradient	totalPressure	Symmetry	fixedFluxPressure
k	fixedValue	inletOutlet	inletOutlet	Symmetry	kqRWallFunction
ω	fixedValue	inletOutlet	inletOutlet	Symmetry	omegaWallFunction
ν_t	fixedValue	zeroGradient	zeroGradient	Symmetry	nutkRoughWallFunction
alpha	fixedValue	variableHeightFlowRate	inletOutlet	Symmetry	zeroGradient
volumeForce	fixedValue	fixedValue	fixedValue	Symmetry	fixedValue

Fig. 5. Coordinate systems and variables from bottom view.

Table 3
Average y^+ and total mesh size for different drift cases.

Parameter	$\beta = -10°$	$\beta = 0°$	$\beta = +10°$
y^+ of hull	1.13	1.05	1.13
y^+ of rudder blade	0.33	0.42	0.34
y^+ of rudder skeg	0.40	0.59	0.39
Total mesh size	15.37 M	16.25 M	15.32 M

L_{pp} forward of KCS FP, and the outlet boundary is positioned at 3.0 L_{pp} aft of the KCS AP. To mitigate the wall's impact on the numerical simulation, both side boundaries are established 1.5 L_{pp} apart from the mid-ship position of the KCS hull. The bottom boundary is positioned 1.5 L_{pp} below the free surface, whereas the top boundary is positioned 1.0 L_{pp} above the free surface. The setup of the computational domain is illustrated in Fig. 6. The selected boundary conditions for this study are listed in Table 2. For the inlet boundary conditions, fixed velocity and zero pressure gradient are used. For the hull and the rudder, a non-slip condition is used for velocity, and zero normal gradient is set for the pressure. At the outlet boundary, a zero gradient condition is used for both velocity and pressure. A slip boundary condition is set for top, sides, and bottom domain boundaries. The volumeForce parameter (Fv) is used to calculate the propeller thrust and torque as the propeller modelling is achieved through body forces without meshing the propeller geometry.

4. Grid generation

The mesh utilities blockMesh and snappyHexMesh from OpenFOAM are used for grid generation. Firstly the computational domain mesh comprised of hexahedral structured mesh is generated using blockMesh, which is also used for the definition and refinement of the free surface region. Then four refinement boxes are employed to gradually refine the grid to enhance the resolution of the structured mesh surrounding the KCS hull and rudder. The cells within these boxes are partitioned in both horizontal and vertical directions. In order to ensure smooth transitions between regions with varying mesh densities, a gradual reduction of the refinement zone is implemented during each level of refinement. In addition, another smaller box is utilized to provide an additional refinement to the mesh in the stern region, which encloses the aft part of the KCS hull, the KCS rudder, and also the propeller region. To accurately capture the dynamics of the boundary layer,

the first cell height is determined based on a target value of y^+=1. The snappyHexMesh utility is employed to add eight prism layers to the surface of the KCS hull and rudder, using an expansion ratio of 1.2 as recommended by ITTC (2014). It should be noted that in cases involving non-zero drift, the aforementioned mesh generation procedures are modified accordingly. The primary adjustments involve rotating the refinement boxes to an angle equal to the degree of drift to make sure that they are aligned with the longitudinal axis of the hull. This can save the total mesh sizes and the associated computational costs. Table 3 displays the average values of y^+ for each component and the corresponding total mesh sizes for three different cases of drift. These values are obtained for KCS in drift motions with a rudder angle of zero degrees ($\beta_r = 0°$). However, the actual values may vary for cases with non-zero rudder angles, although the differences are not significant. Fig. 7 provides a detailed illustration of the grid distribution around the KCS with 0° drift, viewed from the side. Additionally, the figure presents a close-up examination of the discretized computational domain near both the stern and the bow.

4.1. Validation and verification

To guarantee the credibility of numerical simulations, a validation and verification study is carried out for the straight-ahead KCS (zero drift angle) with a zero rudder angle at the ship design Froude number (0.26) under calm water conditions with the freedom to heave and pitch. This scenario aligns with Case 2.1 of KCS from the 2015 Tokyo Computational Fluid Dynamics (CFD) Workshop. An analysis is conducted to assess the sensitivity of grid spacing and time step, employing a methodology based on the works of Stern et al. (2001) and ITTC (2017).

To assess grid sensitivity, three grids are generated, namely, Mesh 1, Mesh 2, and Mesh 3, using a structured background mesh with a systematic refinement factor of 1.1 for the same geometry definition. Table 4 summarizes the grid distribution in x, y z directions and the total mesh size for each grid, along with relevant simulation parameters such as time step, simulation time, and computational costs. Table 5 presents the results obtained by the different grid cases. Table 6 lists the numerical uncertainties of the KCS total resistance coefficient, indicating the simulation results are valid. Similar procedures are also carried out for the time step sensitivity study with three different time steps, $\Delta t_1 = 0.0005$ s, $\Delta t_2 = 0.001$ s and $\Delta t_3 = 0.002$ s for Mesh 3 and details are listed in Table 4. As shown in Fig. 8(b), using a smaller time step does not yield a notable improvement or substantial variation in results. Therefore, the time-step sensitivity study remains validated. Due to the significant increase in the computational cost of using a finer mesh and a smaller time step, Mesh 3 coupled with a timestep of $\Delta t_3 = 0.002$ s is selected for all subsequent computations.
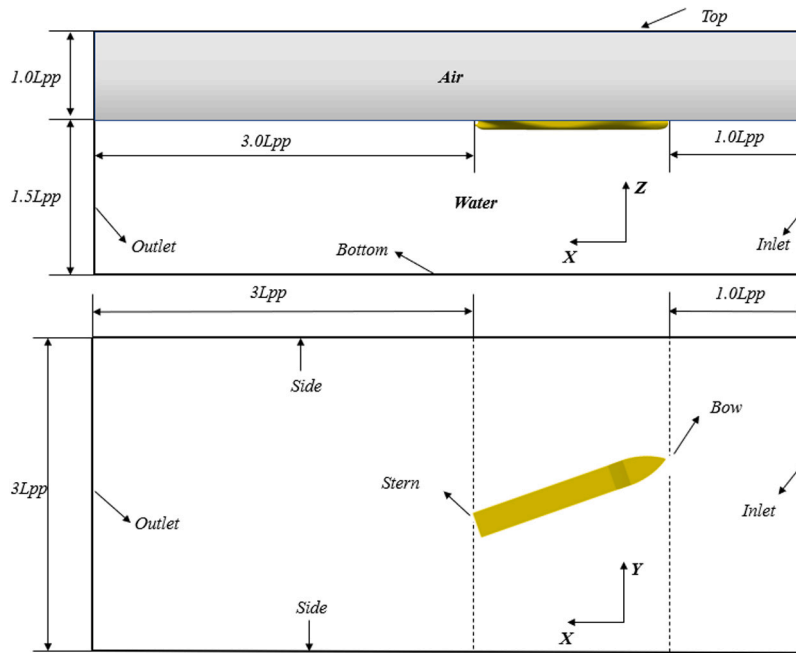
Fig. 6. Computational domain from side and top views.

Table 4
Computational system details for Mesh and Timestep sensitivity study.

Parameter	Mesh			Timestep (Δt)		
	1	2	3	1	2	3
blockMesh refinement	$133 \times 31 \times 48$	$121 \times 28 \times 44$	$110 \times 26 \times 40$	$110 \times 26 \times 40$	$110 \times 26 \times 40$	$110 \times 26 \times 40$
Total cell numbers (M)	26.3	20.5	16.3	16.3	16.3	16.3
Time step (s)	0.002	0.002	0.002	0.0005	0.001	0.002
Simulation Time (s)	35	35	35	35	35	35
Computational cost (h)	75–80	60–65	50–55	205–210	110–115	50–55
Computing system	Iridis 5 Linux Cluster, University of Southampton HPC Facility					
CPUs	Two nodes, 40 cores/node, 192 GB DDR4 memory					

Table 5
Total resistance coefficients of different grids.

Case	Timestep	$C_T/10^{-3}$	Diff.
Mesh1	$\Delta t_3 = 0.002$ s	3.666	−1.2%
Mesh2	$\Delta t_3 = 0.002$ s	3.643	−1.8%
Mesh3	$\Delta t_3 = 0.002$ s	3.613	−2.6%
EFD	–	3.711	–

Table 6
The numerical uncertainties of resistance coefficients of different grids.

Parameter	r_G	R_G	Convergence conditions	C_G	U_{SN} (%D)	E (%D)
Grid	1.1	0.76	monotonic convergence	1.5	3.9	1.2

In addition, hydrodynamic pressure distribution on the free surface at three static drift angles is presented in Fig. 9, demonstrating a good resolution using the selected mesh density and time step, as it was studied in Díaz-Ojeda et al. (2023).

5. Results

5.1. Propeller open water performance

• Zero degree drift scenarios

Fig. 10 presents open water curves of the KCS propeller at straight-ahead condition ($\beta = 0°$) predicted by both BEMt and Yamazaki model and the computed results are compared with experimental data

from Hino et al. (2020). The propeller thrust and torque coefficients, open water efficiency and advance ratio are defined in Eqs. (26) and (27) respectively:

$$K_T = \frac{T}{\rho n^2 D^4} \qquad K_Q = \frac{Q}{\rho n^2 D^5} \tag{26}$$

$$\eta_o = \frac{K_T}{K_Q} \times \frac{J}{2\pi} \qquad J = \frac{U}{n \times D} \tag{27}$$

where T and Q are the calculated propeller thrust and torque, J is the advance ratio, n refers to the number of revolutions and D is the propeller diameter, ρ is the density of water.

Overall, propeller force prediction by both body force models shows good agreement with the experiment. For BEMt, the best agreement of thrust prediction is found where $0.4 < J < 0.8$, and this range covers all considered rpm values in this study. In contrast, the thrust prediction by the Yamazaki model is well predicted for most advance ratios, which could be due to the inclusion of tangential wake effect correction. Both models can accurately capture the open water curves trend with varying propeller advance ratios even though the propeller geometry is represented as simple distributions of pitch and chord rather than the full geometry.
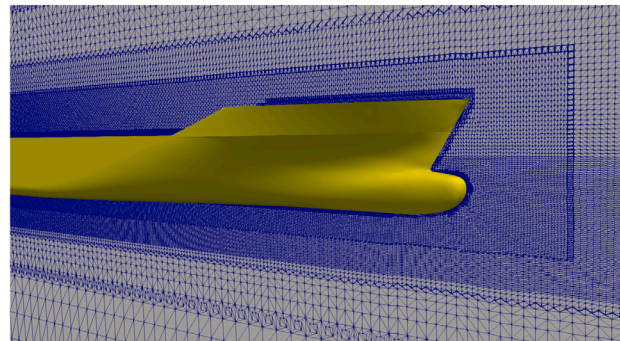
• Non-zero degree drift scenarios

To ensure the credibility of both body force models in oblique conditions, BEMt and Yamazaki models are also adopted to simulate the effective wake of the KCS propeller (Tokyo model scale) subject to a uniform and oblique flow (drift angle β=10°) and the computed
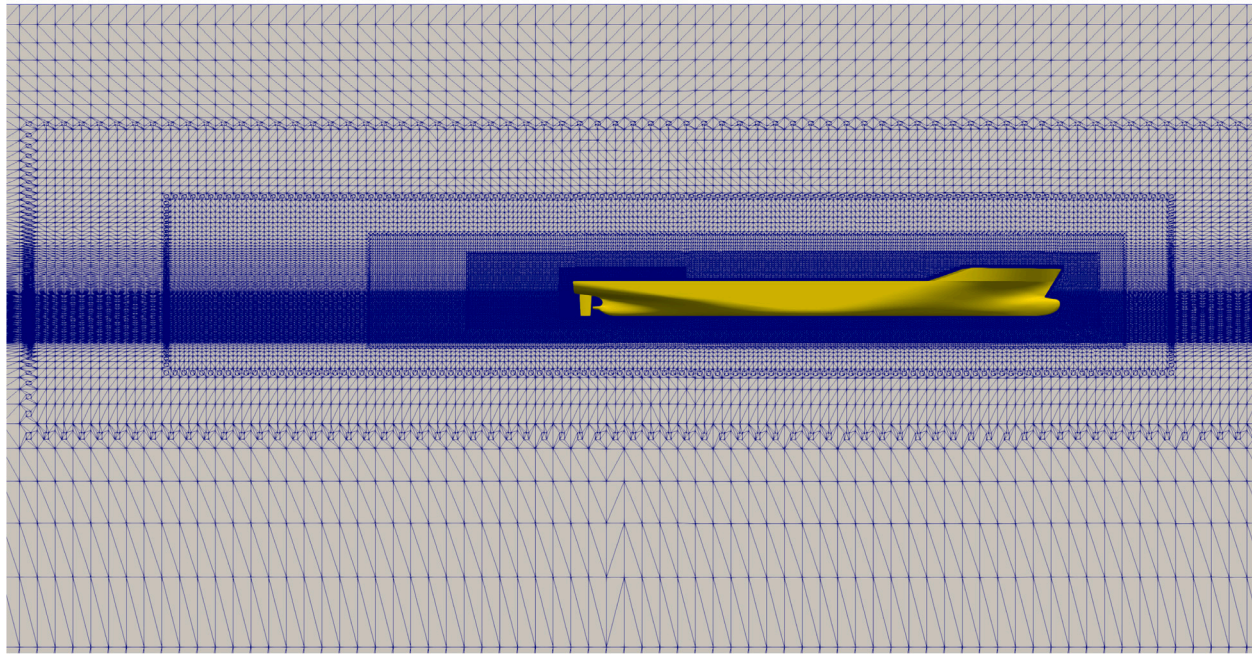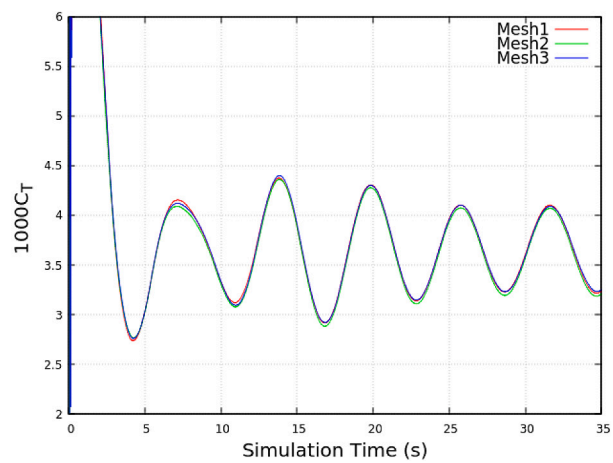
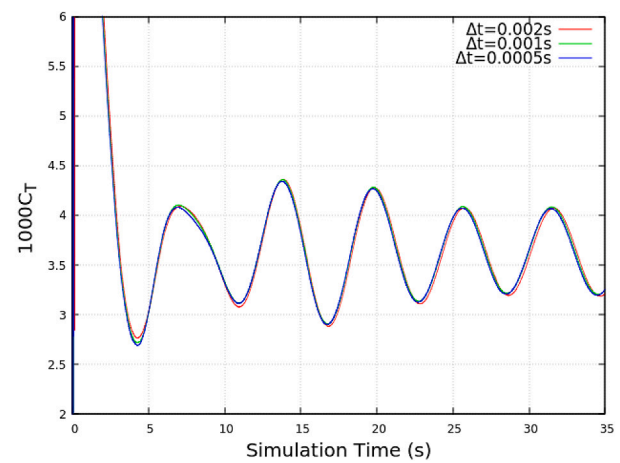(a) Grid distribution from side view
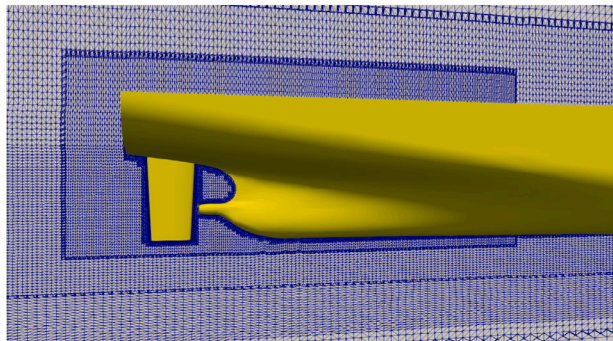
(b) Grid near the stern

(c) Grid near the bow

Fig. 7. Grid distribution around the straight-ahead KCS including rudder.

(a) Different meshes with the same Timestep Δt_3

(b) Different time steps with the same Mesh3

Fig. 8. KCS total resistance coefficient variation with time history for Mesh and Timestep sensitivity study.

(a) $\beta = 0\,^\circ,\ \beta_r = 0\,^\circ$

(b) $\beta = +10\,^\circ,\ \beta_r = 0\,^\circ$

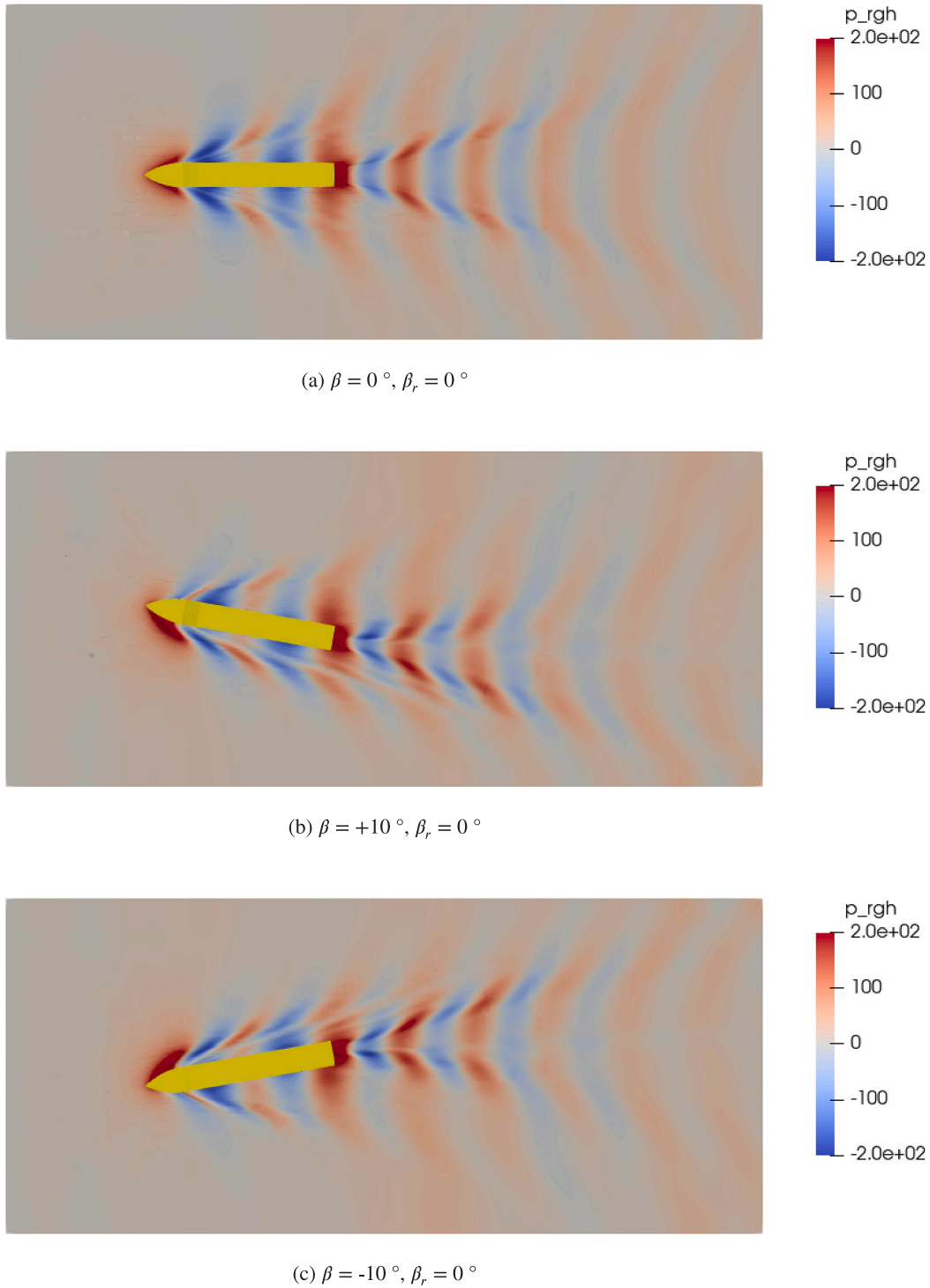(c) $\beta = -10\,^\circ,\ \beta_r = 0\,^\circ$

Fig. 9. Hydrodynamic pressure distribution on the free surface with different drift angles in resistance tests, $Fn = 0.26$.

propeller open water curves in oblique flow are compared with straight-ahead conditions, as shown in Fig. 11, in which K_T, $10K_Q$ and η_0 are still plotted as the function of advance ratio J as defined in Eq. (27). However, the actual advance ratio J_i used in both models is defined as:

$$J_i = \frac{U \times cos\beta}{n \times D} \tag{28}$$

β represents the drift angle, specifically quantified as 10°. Consistency is maintained in the value of n across both non-yawed and yawed conditions, therefore $J_i \neq J$. The comparative analysis between the 0° and 10° scenarios reveals minimal divergence in results. This is

attributed to the fact that the cosine of 10° is approximately 0.985, indicating a very tiny deviation, nearly 99%, from the inflow velocity in a straight-ahead condition. As depicted in Fig. 11, the open water performance curves under the applied drift angle of 10° demonstrate a pattern akin to the straight-ahead condition. However, deviations still are observed, including an upward shift in the propeller thrust and torque coefficients and a corresponding downward shift in open water efficiency within the range of $0.35 < J < 0.8$. These slight shifts are discernible in both the Blade Element Momentum theory (BEMt) and
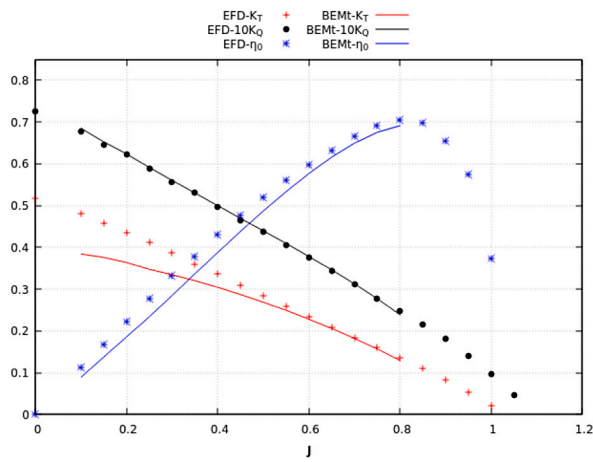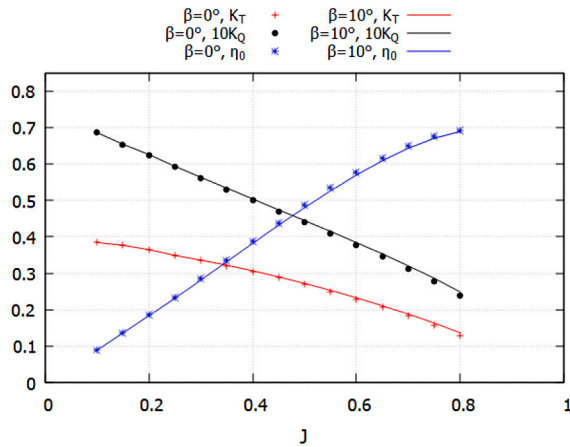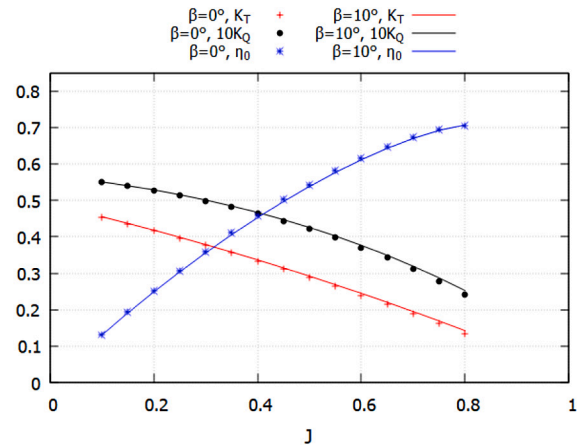
(a) Open water curve predicted by BEMt
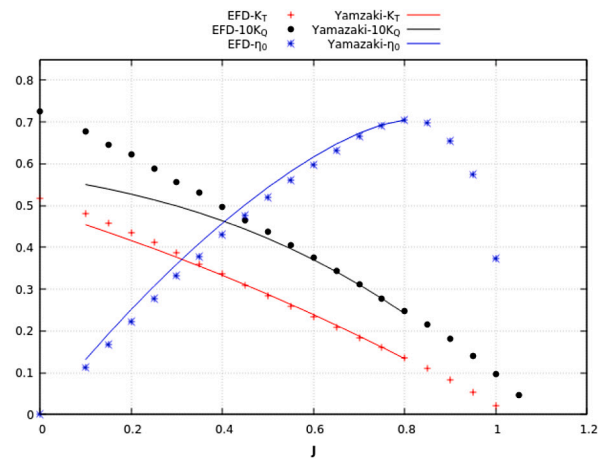
(b) Open water curve predicted by Yamazaki

Fig. 10. Open water performance of the KCS propeller predicted by BEMt and Yamazaki model and compared with EFD from Hino et al. (2020).

(a) Open water test in oblique flow predicted by BEMt

(b) Open water test in oblique flow predicted by Yamazaki

Fig. 11. Propeller open water tests in oblique flow ($\beta = 0°$ and $10°$) predicted by BEMt and Yamazaki model.

Yamazaki models, indicating the nuanced impact of the drift angle on propeller performance.

5.2. Hull–rudder interaction

Fig. 12 presents the influences of drift and rudder angles on the KCS forces, non-dimensional total resistance coefficient C_T, and side force coefficient F'_Y, which includes the forces from the KCS hull and the KCS rudder in calm water at the ship design Froude number of 0.26. To validate the accuracy of numerical results, the KCS of the Southampton model scale (SOTON Model) is adopted to perform the calm water resistance test in the Boldrewood Towing Tank at the University of Southampton. Experimental results used in this study were obtained in September 2022. While a comprehensive explanation of the EFD study is out of the scope of the current study, the detailed setup and tests of experiments can be found in Bowker et al. (2023). The main particulars of the SOTON KCS model are listed in Table 1 and the tank dimensions are 138 *m* in length, 6 *m* in width, and 3.5 *m* in depth. As the CFD and EFD results are obtained using two different model scales' KCS, thus the standard scaling approach is used to fit and scale the total resistance and side force of the SOTON scale to the Toyko scale using the following equations:

$$\text{Ct}_{\text{Tokyo}} - \text{Cf}_{\text{Tokyo}} = \text{Ct}_{\text{soton}} - \text{Cf}_{\text{soton}} \tag{29}$$

$$\text{Fy}_{\text{Tokyo}} = \text{Fy}_{\text{soton}} \tag{30}$$

Overall, both hydrodynamic forces (drag and side forces) present good agreement between EFD and CFD results for all static drift and rudder angles. For zero drift, the drag force increases with the increment of rudder angle, and the C_T is nearly symmetric about the axis of $\beta_r = 0°$. When a non-zero drift angle is applied, the drag force plots of $\beta = -10°$ and $+10°$ shift upwards and the maximum value of C_T occurs at $+20°$ rudder angle for positive drift angle while it is observed at $-20°$ rudder angle for negative drift angle. For $\beta = 0°$ and $+10°$, EFD results are slightly higher than CFD results, mainly because the all-movable rudder type is used in the experiment, therefore inducing more rudder drag force compared to CFD results, in which only the rudder blade is rotatable while the rudder skeg is always fixed. In addition, the bigger deviation between EFD and CFD can be found for larger rudder angles, e.g. $-30°$ and $+30°$. The main possible reason is the effect of increased rudder angles, which makes the fluid around the rudder more turbulent and less streamlined. This could result in flow separation, where the fluid detaches from the rudder surface and forms vortices, which makes CFD more challenging to capture. In terms of the non-dimensional lateral force F'_Y at straight-ahead condition (zero drift angle), the general trend is that the side force increases with the larger absolute value of the rudder angle, and the sign of transverse
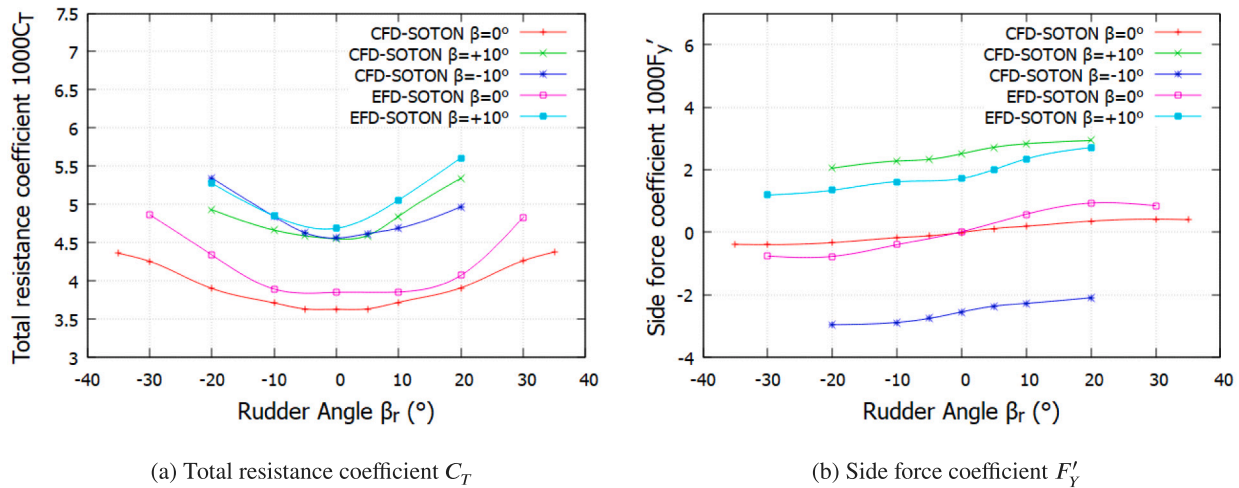
(a) Total resistance coefficient C_T

(b) Side force coefficient F_Y'

Fig. 12. Influence of drift and rudder angles on non-dimensional KCS hull forces and comparison between CFD and EFD.

Table 7
Drag force components of KCS at 0° drift with rudder angles (unit: N).

β_r (°)	Hull R_P	Hull R_V	Rudder R_P	Rudder R_V	R_{Hull}	R_{Rudder}	R_T
−35	9.03	65.91	25.05	0.39	74.94	25.44	100.38
−30	10.91	66.08	20.54	0.43	76.99	20.97	97.96
−20	13.35	66.16	9.60	0.68	79.50	10.28	89.79
−10	14.65	66.11	3.90	0.77	80.76	4.67	85.43
−5	15.05	66.16	1.58	0.81	81.21	2.39	83.60
0	15.39	66.20	1.05	0.84	81.59	1.89	83.48
5	15.05	66.11	1.65	0.82	81.15	2.47	83.62
10	14.59	66.50	3.76	0.77	81.09	4.53	85.62
20	13.34	66.11	9.81	0.72	79.45	10.53	89.98
30	10.87	66.01	20.83	0.43	76.88	21.26	98.14
35	8.95	65.97	25.43	0.39	74.92	25.82	100.73

force is the same as that of rudder angle. Similar to drag force, the side force of EFD at zero drift is slightly larger than CFD results, which can also be attributed to the bigger wetted surface area of the adopted all-movable rudder. When a non-zero drift angle is applied, the lateral force curve slope does not change significantly. However, it is evident that positive and negative drift angles lead to upward and downward shifts, respectively. It is noteworthy that the EFD results for the side force coefficients F_Y' are consistently lower than their CFD counterparts for a drift condition of +10°. A possible explanation is that the actual drift angle in the towing tank test is smaller than 10°, but the overall trends from both EFD and CFD are consistent. In addition, compared to the influence of rudder angle, the effect of drift angle is more notable in lateral force.

Table 7 displays the longitudinal force components comprising the total resistance encountered by KCS when operating in straight-ahead condition ($\beta = 0°$). The result reveals that the hull pressure drag component decreases as the rudder angle increases while the viscous drag component remains relatively constant. This outcome is due to the non-uniform fluid flow upstream of the rudder when a non-zero rudder angle is applied. As a result, the pressure distribution along the length of the hull is altered, leading to a reduction in the net pressure force.

The influence of static drift and rudder angle on rudder forces is demonstrated in Fig. 13. As the rudder angle increases, the rudder force grows owing to the larger angle of attack. When a drift angle is applied, the slope of the rudder drag curve becomes more pronounced than in zero drift cases. In addition, the applied non-zero drift angles result in a vertical shift in the rudder lift curve but have a relatively minor impact on the lift curve slope.

Straight-ahead and 10° drift KCS wave patterns predicted by CFD and EFD from the side view with $Fn = 0.26$ in resistance test are presented in Figs. 14. It can be found that wave elevations generated by

CFD match well with experimental measurement: high elevation occurs at the bow region, followed by a gradual decrease along the hull length, and low elevation can be seen around the amidship. The applied non-zero drift angle not only intensifies the asymmetry of the wave pattern but also develops a tiny high-elevation region near the bow, which is shown in Fig. 14(b). Similarly, Fig. 15 illustrates wave elevations of 10° drift KCS from the bow and stern view: CFD is able to reproduce wave patterns with good similitude when comparing wave pictures between numerical and experimental results, especially the experiment demonstrating that the applied 10° drift angle results in an obvious high wave elevation at the starboard of the bow region and CFD can capture this phenomenon accurately, as presented in Fig. 15(a).

5.3. Hull–propeller–rudder interaction

5.3.1. Influence of drift angle on hull drag

Fig. 16(a) illustrates the calculated KCS total resistance coefficients (C_T) in a straight-ahead condition for five different propeller revolution rates using the BEMt and Yamazaki propeller models. Both BEMt and Yamazaki models exhibit a consistent trend in the variation of the KCS total resistance coefficients (C_T): as the rudder angle magnitude increases, the total drag correspondingly rises. Besides, a higher propeller revolution rate leads to an increased total drag, partially resulting from reduced pressure at the hull's rear. Due to the unidirectional rotation of the propeller, a more substantial drag is observed at a negative, non-zero rudder angle compared to its corresponding positive rudder angle. Overall, a good agreement can be found between BEMt and Yamazaki models. However, their discrepancies become more evident as the propeller revolution rate increases. The KCS total resistance coefficients (C_T) values under non-zero static drifting conditions ($\beta = -10°, +10°$) are provided in Table 8, from which it is found that the C_T values for positive/negative rudder angles get closer to each other for higher RPM for both BEMt and Yamazaki, indicating a reduced dependency of Ct on rudder angle at higher RPM. Additionally, high RPM results in a more obvious flow straightening effect from propeller action, resulting in a decrease in effective inflow angle to the rudder, hence reduction in both rudder drag force and C_T. To examine the influence of the rudder on KCS total resistance at non-zero drift, a comparison is made between the differences in C_T values (dC_T) for drift conditions and zero drift scenarios, as shown in Fig. 16(b). The applied drift angle clearly increases the total ship drag but with an opposite trend for positive and negative drifts: dC_T increases when the rudder angle increases from −20° to +20° for +10° drift angle while the curve of dC_T shows decreasing trend with rudder angles for −10° drift. However, there are some fluctuations between the RPM curves as a

(a) Rudder drag coefficient C_D

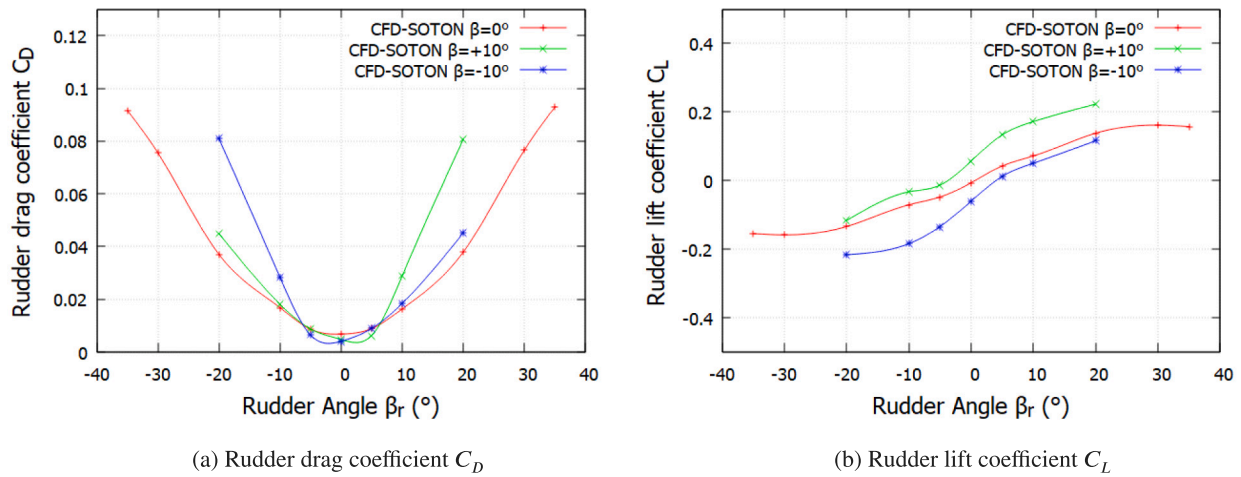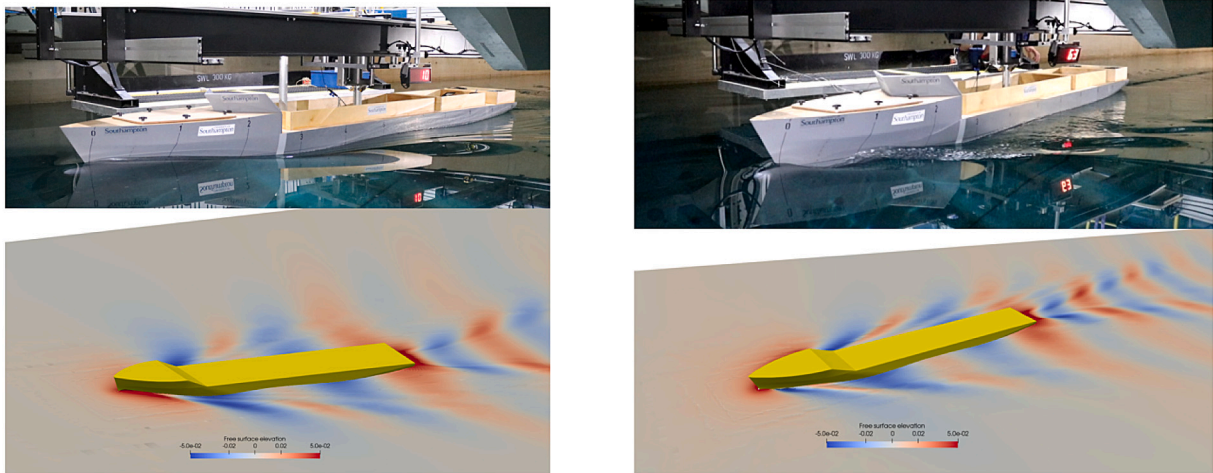(b) Rudder lift coefficient C_L

Fig. 13. Effect of drift and rudder angles on ruder forces.

(a) Wave elevation comparison between EFD and CFD for zero degree drift KCS

(b) Wave elevation comparison between EFD and CFD for ten degree drift KCS

Fig. 14. Wave elevation comparison between EFD and CFD for zero and non-zero drift scenarios from side view, $Fn = 0.26$.

function of the rudder angle, which is more obvious in 16(b). To further validate the accuracy of both body force models in simulating the real flow, the experiments involving propeller action should be taken into account.

### 5.3.2. Influence of drift angle on propeller performance

The computed propeller forces (K_T, $10K_Q$) by BEMt and Yamazaki models for non-zero static drift cases at propeller revolution of 600 rpm are shown in Fig. 17. Both body force models can effectively capture the fluctuations in propeller performance under varying static drift and rudder angle conditions. Furthermore, the propeller performance predictions derived from these models demonstrate a similar pattern. A more substantial discrepancy between the two propeller models is observed in the calculated thrust coefficients in comparison to the propeller torque coefficients. This could be due to the fact that the BEMt lacks the capacity to properly account for tangential inflow velocities compared to the Yamazaki model. This may also explain the reason why BEMt results show more symmetry than those obtained by Yamazaki model. Table 9 lists the propeller thrust and torque arguments (dK_T, d10K_Q), derived by evaluating the net change in propeller forces between the drift ($\beta = -10°$, $+10°$) and zero-drift

($\beta = 0°$) scenarios. In comparison to cases with a $-10°$ drift angle, the propeller performance tends to experience a greater deterioration when subjected to a $+10°$ drift angle at corresponding rudder angles. A possible explanation is that positive drift angles may induce more flow separation and turbulence around the propeller, resulting in a more negative impact on thrust and torque generated by the propeller. Besides, the propeller operating at a positive drift angle may cause unfavourable flow interaction with the downstream rudder, leading to a more significant decrease in propeller performance.

Fig. 18 presents the axial velocity contours at cross-section $x/Lpp = 0.9911$ in three drift conditions with rpm = 600, $\beta_r = 0°$, predicted by BEMt and Yamazaki model. Both body force models can accurately capture the influence of drift angle on local axial velocity and the contour's patterns and values show good similarity. In addition, local velocity profiles downstream of the propeller plane $x/Lpp = 0.9911$ at $z/Lpp = -0.03$ for three drift scenarios predicted by both propeller models are shown in Fig. 19. All plots are not continuous around the $y/L_{pp} = 0$ due to the presence of the rudder. The distribution of velocities predicted by two body force models shows good agreement, in particular for the straight-ahead case. In non-zero drift conditions, differences are mainly observed for the propeller axial velocities (u
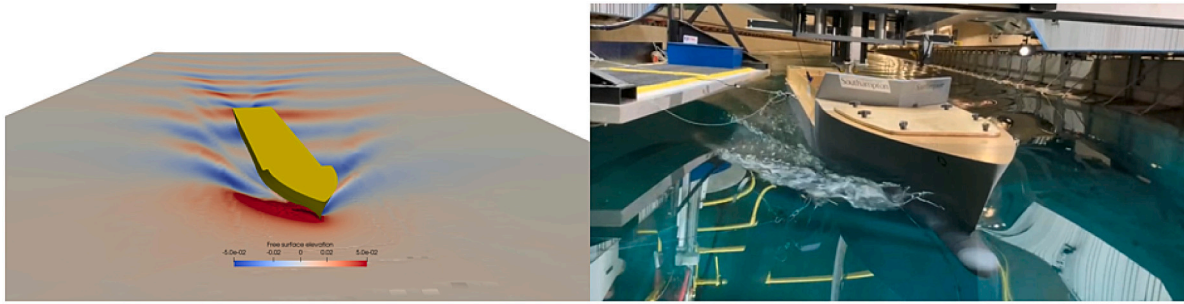
(a) Wave elevation at bow of CFD and experiment for KCS at angle drift of 10 °
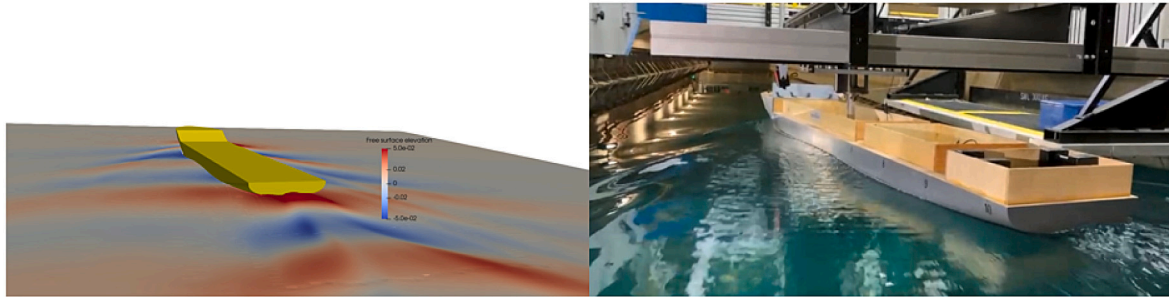
(b) Wave elevation at stern of CFD and experiment for KCS at angle drift of 10 °

Fig. 15. Wave elevation of CFD and experiment for KCS at angle drift of 10° at bow and stern, $Fn = 0.26$.
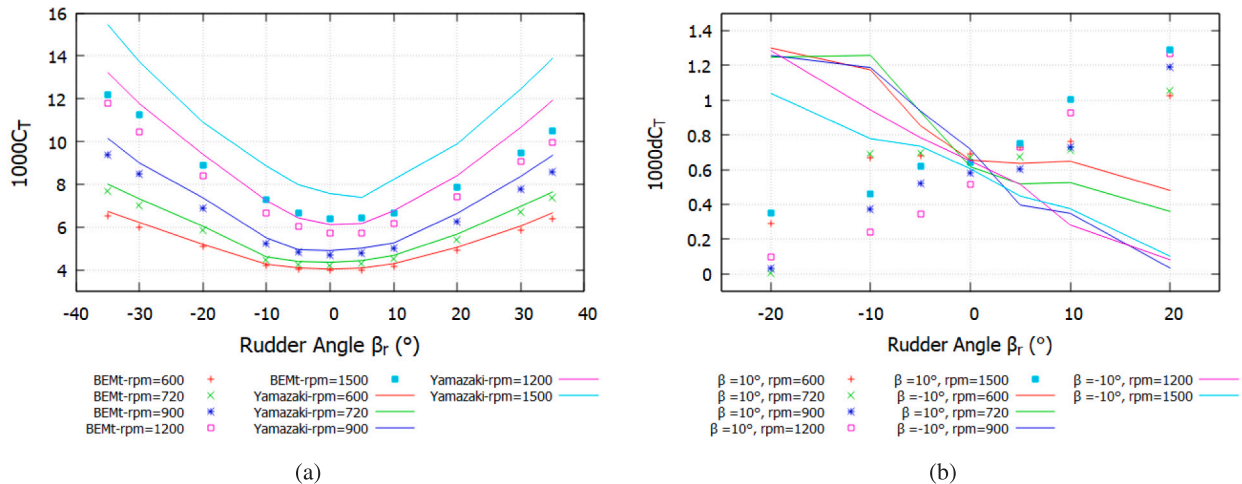

(a)

(b)

Fig. 16. (a):Zero drift KCS's C_T predicted by BEMt and Yamazaki under five different propeller revolutions' conditions; (b):Effect of drift angle on hull drag augments, predicted by BEMt.

plots) near the rudder blade surface region: $0 < y/Lpp < 0.01$ for +10° drift while $-0.01 < y/Lpp < 0$ for −10° drift. The possible reason is that the BEMt model does not deal well with the effects of the tangential wake compared to the Yamazaki model.

5.3.3. Drift angle influence on rudder forces

The impact of drift on rudder force at a propeller revolution rate of 600 rpm is illustrated in Fig. 20. It is found that the presence of a non-zero drift angle exacerbates the asymmetry of the C_D curve. However, it is noteworthy that the minimum rudder drag value consistently occurs at $\beta_r = 0°$ for all three drift scenarios. Furthermore, the introduction of +10° and −10° drift leads to upward and downward displacements, respectively, in relation to the lift curve with zero drift.

Fig. 21 displays the impact of propeller revolution on rudder performance at both positive and negative drift angles, as predicted by the BEMt and Yamazaki models. In general, the rudder performance calculated by both models demonstrates strong agreement for rudder lift across all scenarios, as well as rudder drag in the majority of cases, except for the highest propeller revolution rate of 1500 rpm. This discrepancy arises due to the Yamazaki model's overestimation of propeller forces in comparison to the BEMt model, which consequently results in an augmented inflow velocity to the rudder and an increased rudder drag. At +10° drift angle, the asymmetry of the C_D curves diminishes as the propeller revolution rate increases, which could be attributable to the enhanced flow straightening effects of the propeller. The lift curve C_L slope exhibits an increasing trend as the rpm varies from 600 to 1200. However, the rudder lift declines when the rpm
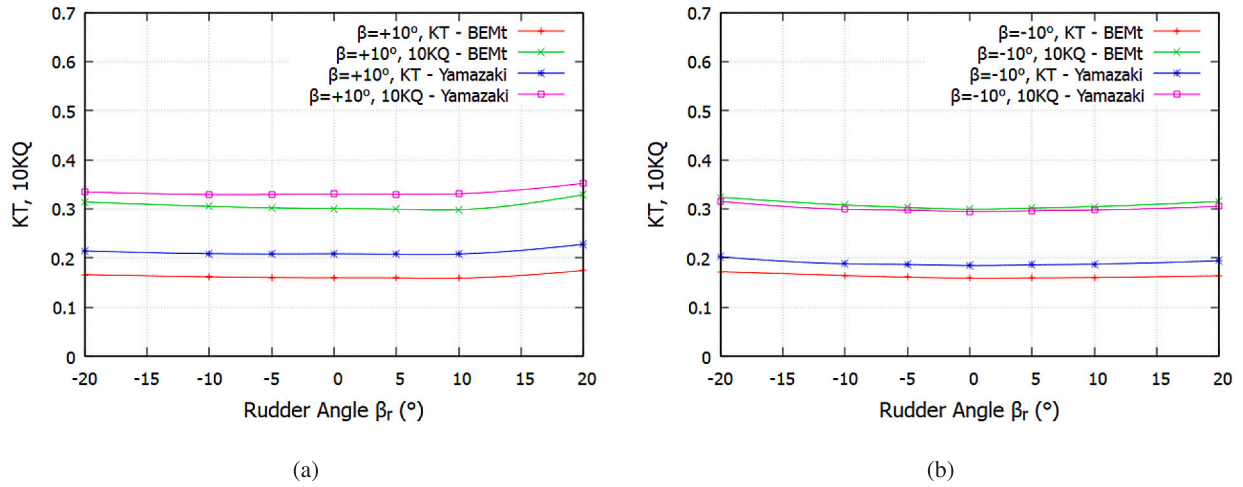
(a)

(b)

Fig. 17. (a):Propeller forces predicted by BEMt and Yamazaki at +10° drift, 600 rpm; (b):Propeller forces predicted by BEMt and Yamazaki at −10° drift, 600 rpm.

(a) $\beta = 0°$, BEMt

(b) $\beta = 0°$, Yamazaki

(c) $\beta = +10°$, BEMt

(d) $\beta = +10°$, Yamazaki

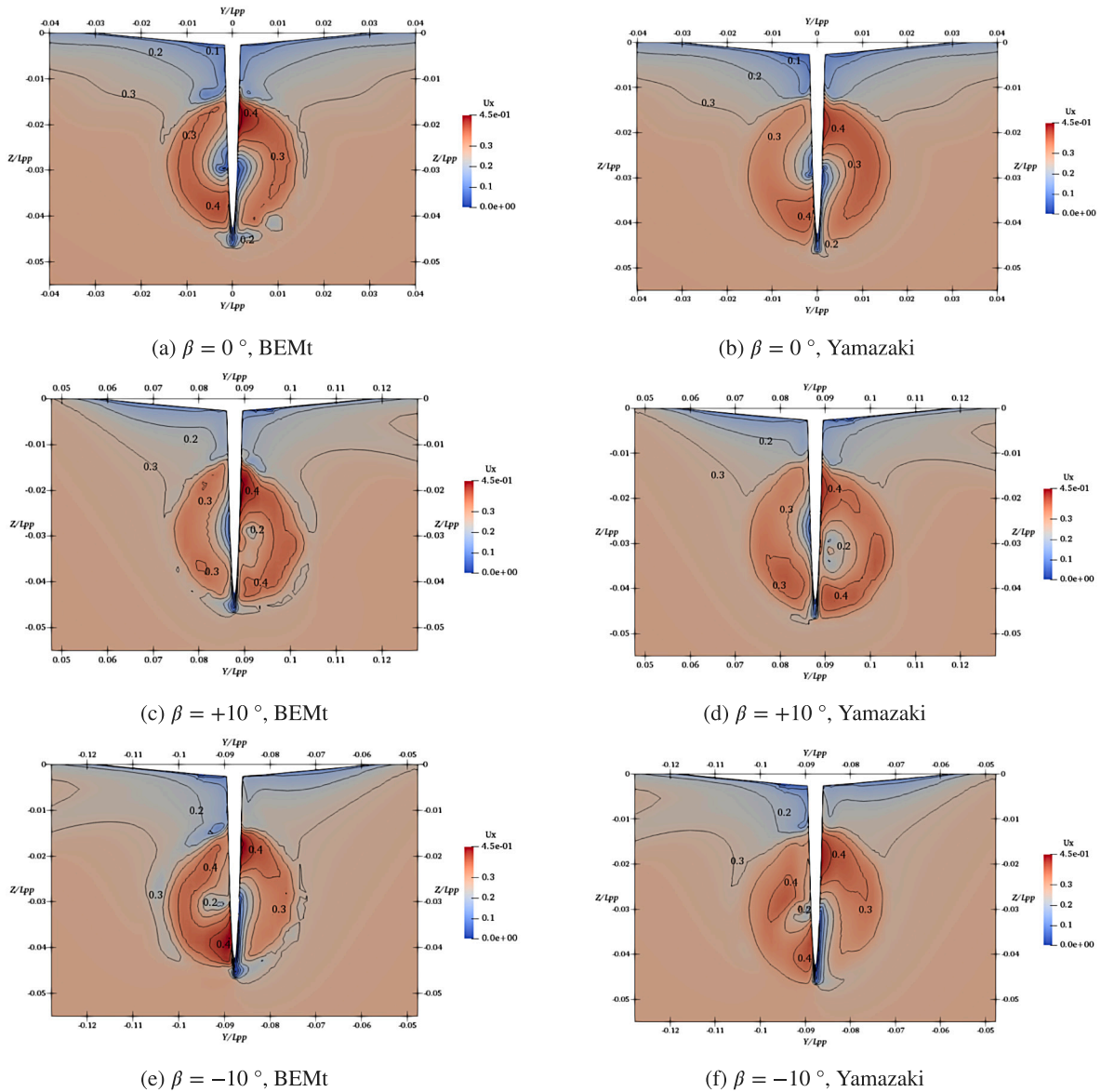(e) $\beta = -10°$, BEMt

(f) $\beta = -10°$, Yamazaki

Fig. 18. Local axial flow contours (U_X) behind the KCS propeller at $x/Lpp = 0.9911$ for three drift scenarios with zero rudder angle, predicted by BEMt and Yamazaki models, rpm = 600.

Table 8

Total drag coefficient at drift angles +10° and −10°, predicted by BEMt and Yamazaki under five different propeller revolutions' conditions.

		BEMt					Yamazaki				
	rpm	600	720	900	1200	1500	600	720	900	1200	1500
β_r	β	Ct	Ct	Ct	Ct	Ct	Ct	Ct	Ct	Ct	Ct
−20°	+10°	5.394	5.853	6.916	8.517	9.242	5.563	6.121	7.430	9.448	11.103
−10°	+10°	4.861	5.151	5.600	6.902	7.730	4.998	5.377	5.987	7.425	9.056
−5°	+10°	4.701	4.955	5.347	6.389	7.257	4.840	5.187	5.738	6.871	8.269
0°	+10°	4.659	4.895	5.278	6.224	7.015	4.788	5.124	5.647	6.698	7.969
5°	+10°	4.728	4.969	5.394	6.458	7.167	4.868	5.197	5.776	6.899	8.085
10°	+10°	4.929	5.212	5.749	7.078	7.680	5.063	5.425	6.115	7.272	8.675
20°	+10°	5.956	6.487	7.468	8.704	9.151	6.076	6.781	7.875	9.635	11.131
-20°	−10°	6.403	7.095	8.143*	9.702	9.931	6.434	7.161	8.327	10.208	11.724
−10°	−10°	5.367	5.715	6.415	7.606	8.046	5.348	5.712	6.431	7.865	9.223
−5°	−10°	4.872	5.187	5.762	6.827	7.373	4.949	5.237	5.769	7.085	8.401
0°	−10°	4.623	4.843	5.413	6.356	6.980	4.717	4.923	5.391	6.629	7.927
5°	−10°	4.636	4.815	5.185	6.245	6.865	4.729	4.948	5.373	6.492	8.081
10	−10°	4.816	5.024	5.366	6.433	7.050	4.929	5.172	5.637	6.849	8.426
20°	−10°	5.411	5.790	6.314	7.519	7.966	5.522	5.965	6.704	8.163	9.789

Table 9

Propeller thrust and torque augments at drift angles +10° and −10°, predicted by BEMt under five different propeller revolutions' conditions.

	rpm	600	720	900	1200	1500	600	720	900	1200	1500
β_r	β	dK_T	dK_T	dK_T	dK_T	dK_T	$d10K_Q$	$d10K_Q$	$d10K_Q$	$d10K_Q$	$d10K_Q$
−20°	+10°	−0.008	−0.006	−0.002	−0.005	−0.005	−0.015	−0.019	−0.018	−0.011	−0.027
−10°	+10°	−0.002	−0.001	−0.002	−0.005	−0.005	−0.002	−0.005	−0.014	−0.011	−0.026
−5°	+10°	−0.002	−0.001	−0.001	−0.005	−0.005	−0.003	−0.005	−0.013	−0.012	−0.024
0°	+10°	−0.002	−0.001	0.000	−0.005	−0.005	−0.003	−0.006	−0.012	−0.011	−0.025
5°	+10°	−0.003	−0.001	−0.001	−0.004	−0.005	−0.005	−0.006	−0.013	−0.009	−0.023
10°	+10°	−0.004	−0.002	−0.001	−0.004	−0.005	−0.007	−0.005	−0.013	−0.010	−0.021
20°	+10°	0.006	0.002	−0.001	−0.005	−0.005	0.010	0.004	−0.009	−0.013	−0.025
−20°	−10°	−0.002	−0.004	−0.005	−0.001	0.003	−0.006	−0.009	−0.014	−0.004	0.048
−10°	−10°	0.001	−0.001	−0.005	−0.002	0.004	0.001	0.000	−0.009	−0.003	0.047
−5°	−10°	−0.002	−0.003	−0.005	−0.002	0.004	−0.002	0.000	−0.009	−0.006	0.048
0°	−10°	−0.003	−0.004	−0.005	−0.002	0.004	−0.004	−0.003	−0.008	−0.005	0.051
5°	−10°	−0.003	−0.004	−0.006	−0.002	0.004	−0.003	−0.003	−0.012	−0.006	0.051
10°	−10°	−0.002	−0.004	−0.007	−0.003	0.004	0.000	0.000	−0.011	−0.008	0.050
20°	−10°	−0.005	−0.007	−0.009	−0.003	0.004	−0.004	−0.003	−0.017	−0.011	0.048

reaches 1500, suggesting that the rudder likely stalls between 1200 and 1500 rpm. In the case of −10° drift conditions, noticeably higher rudder drag values are observed at negative rudder angles for all propeller revolutions. The lift curves exhibit a variation trend similar to that of the +10° drift condition. The impact of drift on rudder performance, as explored in this study, demonstrates good concordance with both experimental data from Molland and Turnock (1995) and numerical results presented by Badoe et al. (2015), in which the influence of drift on the performance of a rudder situated downstream of three different centreboard configurations is investigated.

5.3.4. Influence of drift angle on the hull–propeller-wake interaction

Thrust deduction and wake fraction are two important parameters used to measure the hull–propeller and hull-wake interactions and they are defined in Eq. (31), in which R_{tow} is the resistance during the resistance test, R_{prop} is the resistance during the fixed RPM test, n is the rotation rate, the equivalent behind-hull advance ration J_i is derived from the open water results. The hull efficiency η_H is defined as the ratio of $1 − t$ and $1 − \omega_t$. The interaction effect parameters $1 − t$ and $1 − \omega_t$ play a vital role in the hull efficiency and, subsequently the overall propulsive efficiency of the ship. In order to investigate the impact of static drift and rudder angle on the interaction effects between the hull, propeller, and wake, Table 10 presents the thrust deduction and wake fraction for all considered cases. In addition, the hull efficiency η_H for three drift scenarios are plotted in Fig. 22. It is found that the optimal hull efficiency occurs at zero rudder angle ($\beta_r = 0°$) for all propeller revolution rates when the drift angle is 0° and +10°. Conversely, under −10° drift conditions, the hull efficiency reaches its peak at an approximate rudder angle of +5°.

$$1 - t = \frac{T + R_{\text{tow}} - R_{\text{prop}}}{T} \qquad 1 - \omega_t = \frac{V_{\text{prop}}}{V_{\text{ship}}} = \frac{J_i D_p n}{V_{\text{ship}}} \qquad (31)$$

6. Conclusions

The present study demonstrates the effectiveness of a numerical approach to predict the powering and manoeuvring performance of a fully appended container ship (KCS model) under static drift angles in conjunction with a series of rudder angles using the open-source unsteady Reynolds-averaged Navier–Stokes (URANS) solver OpenFOAM.

Based on the literature review conducted in Section 1, previous studies mainly focused on drift or rudder angles' effect on side force, yaw moment of the hull, which are insufficient to provide a comprehensive understanding of complex interaction at the vessel stern between its propulsors, manoeuvring devices and wake flow (Bowker et al., 2023). Additionally, direct CFD simulations for ship manoeuvring are computationally intensive and the key challenge associated with computations is the validation process, and the acquisition of high-quality experimental data is very difficult and costly (Zhang, 2023). Therefore, this paper aims to provide a step towards a better understanding of ship manoeuvring in real sea states by simulating the fully appended KCS model under conditions of combined drift and rudder angles. This can represent quasi-static phases of an actual ship manoeuvre and removes the need for modelling the complete time-varying manoeuvre, which provides a great reduction in the computational effort, and also a reference for experimental measurement of the hull and its appendages' forces when ships operating at the angle of drift.
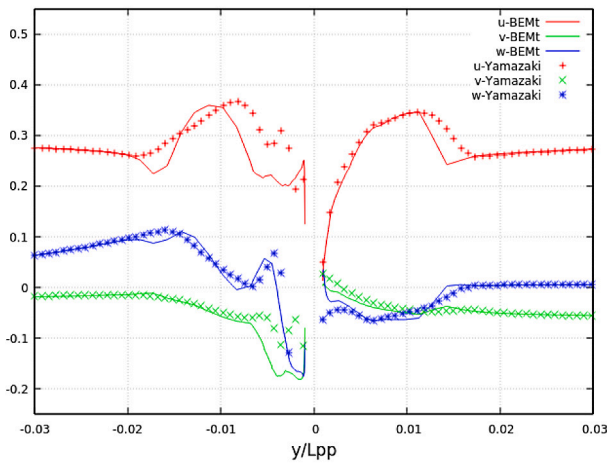
For all considered cases, resistance tests at ship design speed are carried out first and then a series of fixed RPM tests are performed subsequently. Numerical propeller modelling is achieved by using two body force models: Blade Element Momentum Theory (BEMt) and the Yamazaki model, in which the KCS propeller geometry is represented
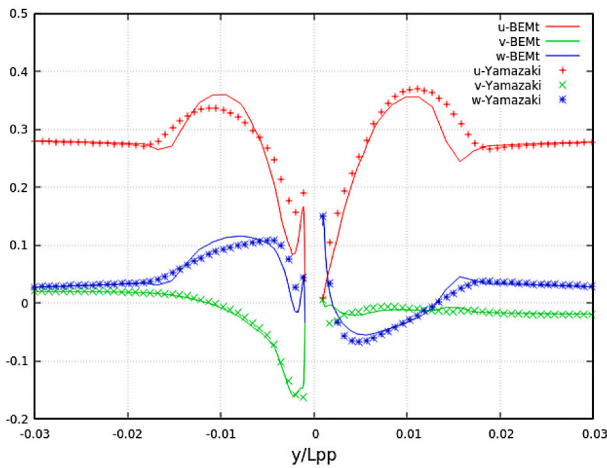
(a) $\beta=0\degree$, $\beta_r=0\degree$
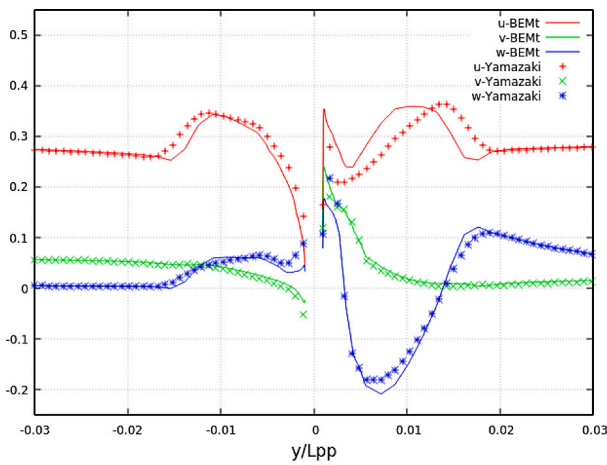
(b) $\beta=+10\degree$, $\beta_r=0\degree$

(c) $\beta=-10\degree$, $\beta_r=0\degree$

Fig. 19. Influence of drift angle on local velocity profiles at $x/Lpp = 0.9911$, $\beta_r = 0\degree$, rpm = 600, predicted by BEMt and Yamazaki models.

as simple distributions of pitch and chord rather than the full geometry. Both models include both axial and circumferential body forces. To validate the accuracy of computational results obtained from the CFD approach, the Southampton KCS model scale is used to perform resistance tests in some drift conditions. The key findings of this study are summarized as follows:

Table 10
Thrust deduction and wake fraction in three drift conditions, predicted by BEMt under five different RPM.

	β_r (°)	$\beta = 0\degree$	$\beta = +10\degree$	$\beta = -10\degree$	$\beta = 0\degree$	$\beta = +10\degree$	$\beta = -10\degree$
		$1-t$	$1-t$	$1-t$	$1-\omega_t$	$1-\omega_t$	$1-\omega_t$
600 rpm	−20	0.593	0.836	0.637	0.826	0.846	0.832
	−10	0.826	0.928	0.812	0.852	0.856	0.850
	−5	0.859	0.959	0.910	0.854	0.859	0.858
	0	0.875	0.960	0.977	0.856	0.860	0.862
	5	0.866	0.950	0.993	0.855	0.861	0.861
	10	0.837	0.969	0.953	0.854	0.862	0.859
	20	0.643	0.792	0.841	0.840	0.826	0.851
720 rpm	−20	0.620	0.815	0.653	0.893	0.909	0.903
	−10	0.848	0.901	0.822	0.915	0.919	0.920
	−5	0.873	0.925	0.885	0.918	0.921	0.925
	0	0.877	0.929	0.941	0.919	0.923	0.930
	5	0.864	0.923	0.959	0.919	0.923	0.930
	10	0.841	0.924	0.930	0.919	0.924	0.930
	20	0.697	0.775	0.831	0.905	0.898	0.924
900 rpm	−20	0.675	0.782	0.689	1.008	1.017	1.026
	−10	0.832	0.896	0.823	1.023	1.029	1.039
	−5	0.867	0.915	0.871	1.030	1.033	1.047
	0	0.880	0.918	0.902	1.033	1.035	1.051
	5	0.871	0.910	0.935	1.032	1.034	1.054
	10	0.855	0.899	0.922	1.030	1.034	1.056
	20	0.739	0.766	0.846	1.018	1.020	1.049
1200 rpm	−20	0.756	0.803	0.764	1.195	1.216	1.201
	−10	0.840	0.876	0.849	1.203	1.226	1.212
	−5	0.869	0.900	0.879	1.208	1.231	1.217
	0	0.886	0.907	0.901	1.212	1.234	1.221
	5	0.885	0.897	0.910	1.211	1.231	1.222
	10	0.867	0.876	0.904	1.209	1.229	1.223
	20	0.808	0.814	0.860	1.206	1.227	1.219
1500 rpm	−20	0.856	0.874	0.869	1.186	1.215	1.166
	−10	0.897	0.910	0.908	1.188	1.218	1.167
	−5	0.913	0.922	0.921	1.190	1.219	1.168
	0	0.920	0.927	0.931	1.192	1.223	1.169
	5	0.919	0.924	0.936	1.194	1.223	1.169
	10	0.914	0.916	0.932	1.194	1.224	1.170
	20	0.885	0.888	0.914	1.194	1.225	1.171

- The influence of drift angle on the hull–propeller–rudder-wake interaction is demonstrated numerically: When the non-zero drift angle is applied, the drag, and lateral force experienced by the hull increase with the increasing rudder angle magnitude. The presence of the rotating propeller tends to intensify this increasing trend. Meanwhile, the rudder forces are mainly dependent on the upstream propeller performance. Higher propeller loading tends to shift the rudder lift and can delay the rudder stall.
- Computational results of both global and local flow characteristics in drift conditions derived from the BEMt and Yamazaki model show good agreement. There is still some uncertainty in predicting propeller forces (and the effective wake) in oblique flows using body force models, especially at high RPMs. However, the main benefit of using simplified body force models is that they provide a large reduction in computational costs compared to the fully discretized propeller method.
- Good agreement is found between experimental and numerical results when predicting hull forces in drift conditions. Comparison of wave patterns generated by EFD and CFD also shows high similitude. This further validates the accuracy of CFD methods and provides a good reference for future validation of actual dynamic manoeuvring simulations.
- Variation of rudder angles has a more obvious influence on the hull efficiency at the straight-ahead condition compared to yawed conditions. Both non-zero drift and higher propeller loading weaken this effect, especially at the positive drift angle. The applied drift angle can also affect the rudder angle position at optimal hull efficiency: 0° rudder angle for zero and positive drift cases while +5° rudder angle for negative drift scenarios.

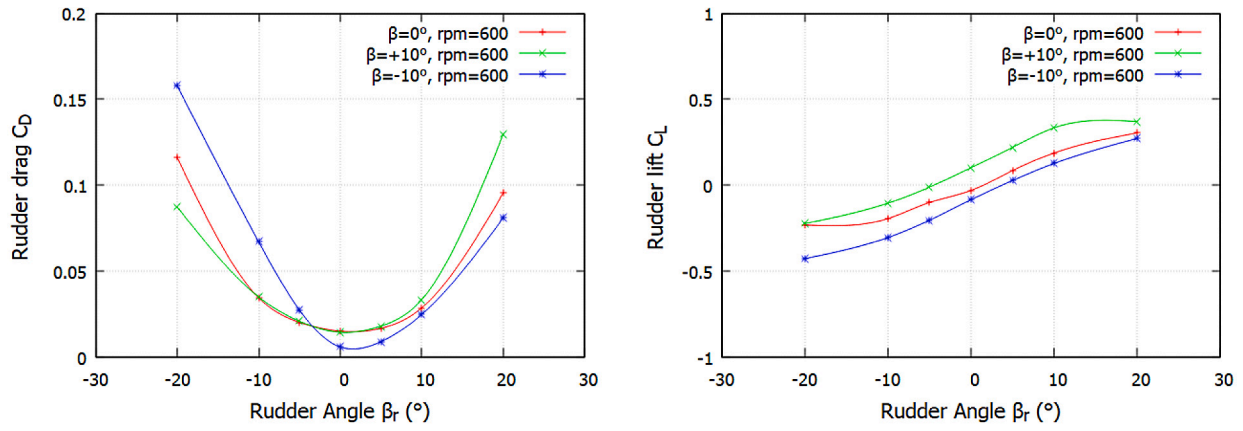**Fig. 20.** Influence of drift angle on KCS rudder force, predicted by BEMt, 600 rpm.
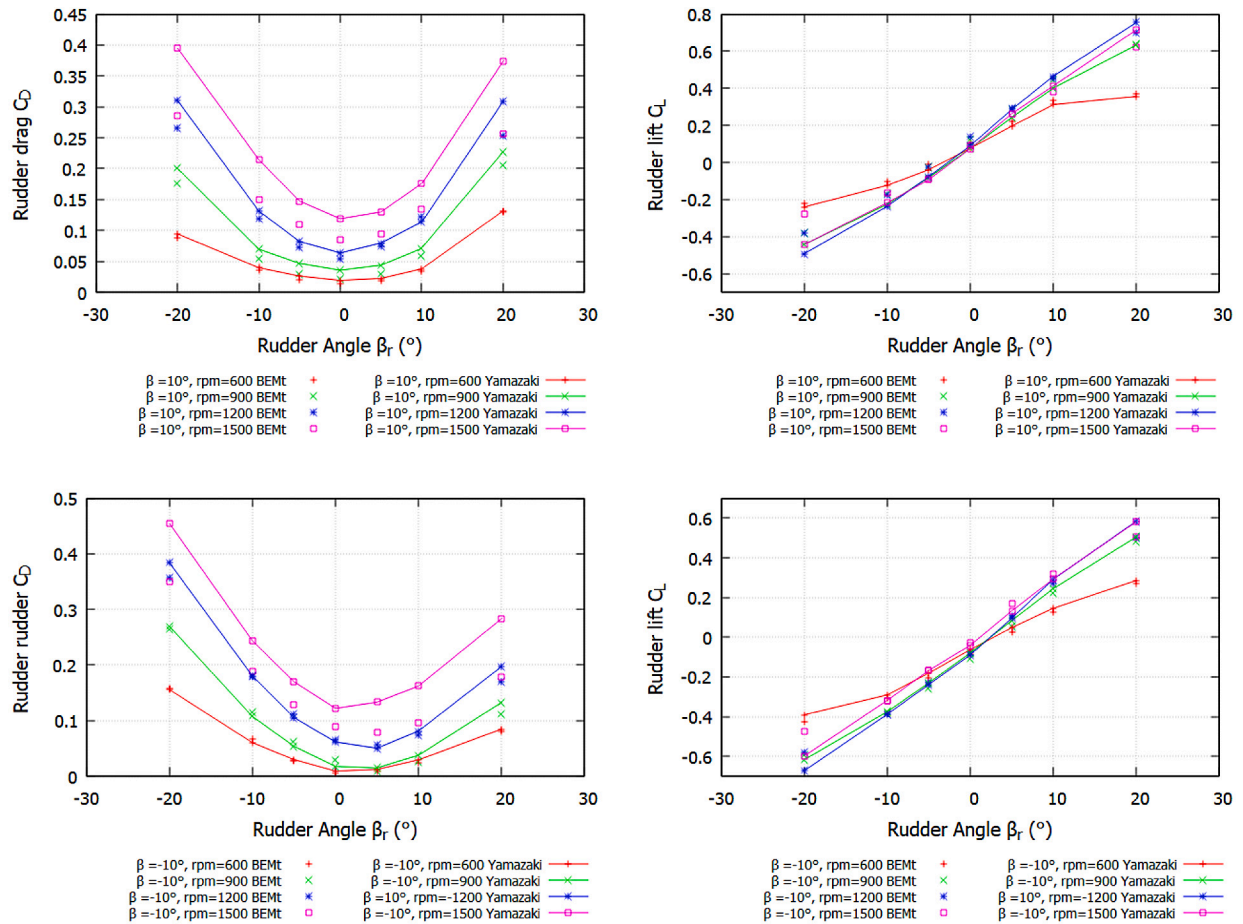

Fig. 21. Effect of propeller revolution on rudder force predicted by BEMt and Yamazaki in +10° and −10° drift angle scenarios.

- The specific verification of the effective wake of propeller alone in oblique flow conducted in Section 5.1 provides insight into the expected numerical errors of body force propeller models in oblique flows. While both models capture the general trend of propeller performance degradation in oblique flow, it should be noted that comprehensive validation with experimental data is still required to fine-tune the model and quantify the exact nature of numerical errors. This verification exercise has elucidated both the BEMt and Yamazaki models' predictive capabilities and established a better understanding of the limitations inherent to actuator disk models in oblique flows.

In conclusion, this work facilitates an enhanced understanding of ship manoeuvring in waves by investigating the influence of drift and rudder angles on the hull–propeller–rudder-wake interaction. This also contributes to a more accurate prediction of the effective wake in oblique flows and a comprehensive understanding of the sensitivity of the results to the chosen propeller models and indications of model limitations. Potential future work should include the acquisition of high-quality experimental data to achieve full validation and verification. Another is to carry out simulations of full-scale vessels, which could extend the practical applications of ship manoeuvring in real sea states.
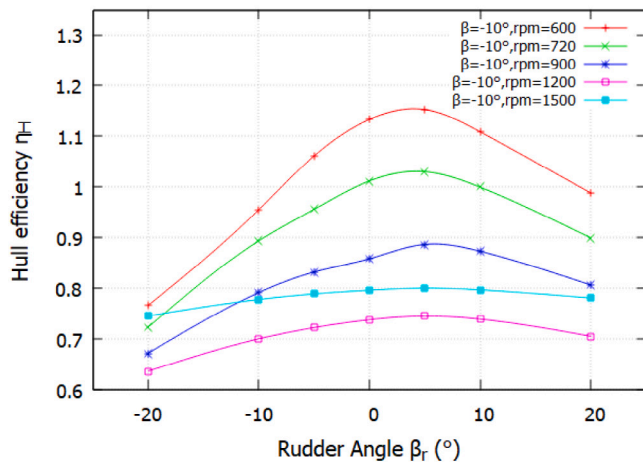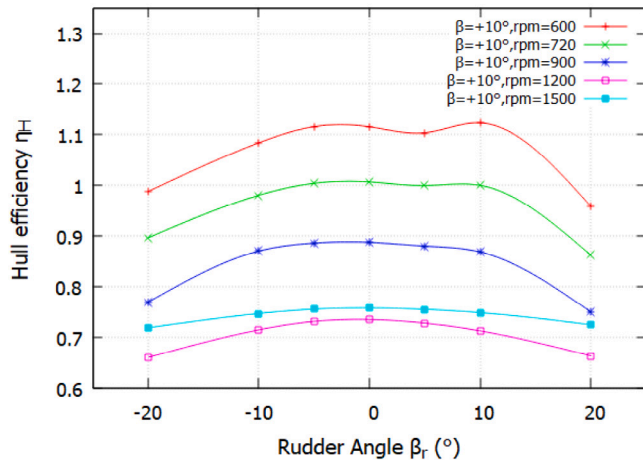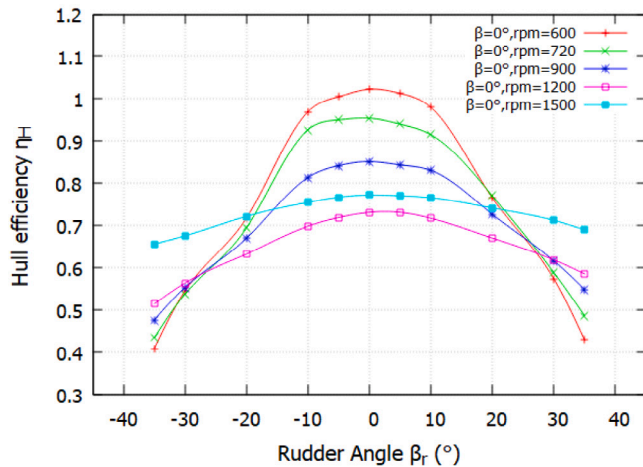
Fig. 22. Top: Hull efficiency η_H at 0° drift; Middle:Hull efficiency η_H at +10° drift; Bottom: Hull efficiency η_H at −10° drift.

References

Badoe, C.E., 2015. Design Practice for the Stern Hull of a Future Twin-Skeg Ship Using a High Fidwlity Numerical Approach (Ph.D. thesis). University of Southampton, pp. 1–226, URL https://eprints.soton.ac.uk/376987//.

Badoe, C.E., Phillips, A.B., Turnock, S.R., 2015. Influence of drift angle on the computation of hull–propeller–rudder interaction. Ocean Eng. 103, 64–77.

Bowker, J., Buckland, D., Gregory, M., Townsend, N., Zhang, Y., Turnock, S., 2023. A free running instrumented container ship model for investigating energy efficiency while manoeuvring in waves. In: The 7thInternational Conference on Advanced Model Measurement Technology for the Maritime Industry. (AMT'23), Istanbul, Turkey.

Burrill, L., 1944. Calculation of marine propeller performance characteristics. Trans. NECIES 60.

Díaz-Ojeda, H., Pérez-Arribas, F., Turnock, S.R., 2023. The influence of dihedral bulbous bows on the resistance of small fishing vessels: A numerical study. Ocean Eng. 281, 114661.

El Moctar, O., 2001. Numerical computations of flow forces in ship manoeuvring. Ship Technol. Res. 48 (3), 98–123.

Goldstein, S., 1929. On the vortex theory of screw propellers. Proc. R. Soc. London Ser. A 123 (792), 440–465.

Hino, T., Stern, F., Larsson, L., Visonneau, M., Hirata, N., Kim, J., 2020. Numerical Ship Hydrodynamics: An Assessment of the Tokyo 2015 Workshop, Vol. 94. Springer Nature.

International Maritime Organization, 2002. Resolution msc. 137(76) standards for ship manoeuvrability.

ITTC, 2014. ITTC–Recommended procedures and guidelines-practical guidelines for ship CFD applications. 7.5-03-02-03 (Revision 01). ITTC-Recomm. Proced. Guidel. 19.

ITTC, 2017. Recommended procedures and guidelines, 7.5-03-01-01, uncertainty analysis in CFD verification and validation methodology and procedures.

ITTC, 2021. The Specialist Committee on Manoeuvring in Waves - Final Report and Recommendations to the 29th ITTC. Tech. rep..

Jiang, L., Yao, J., Liu, Z., 2022. Comparison between the RANS simulations of double-body flow and water–air flow around a ship in static drift and circle motions. J. Mar. Sci. Eng. 10 (7), 970.

Larsson, L., Stern, F., Visonneau, M., 2013. Numerical Ship Hydrodynamics - An Assessment of the Gothenburg 2010 Workshop. Springer Science & Business Media.

Longo, J., Stern, F., 2002. Effects of drift angle on model ship flow. Exp. Fluids 32 (5), 558–569.

Menter, F.R., 1994. Two-equation eddy-viscosity turbulence models for engineering applications. AIAA J. http://dx.doi.org/10.2514/3.12149.

Molland, A., Turnock, S., 1995. Wind Tunnel Tests on the Effect of a Ship Hull on Rudder-Propeller Performance at Different Angles of Drift. University of Southampton.

Molland, A., Turnock, S., 2002. Flow straightening effects on a ship rudder due to upstream propeller and hull. Int. Shipbuild. Prog. 49 (3), 195–214.

Molland, A.F., Turnock, S.R., Hudson, D.A., 2017. Ship resistance and propulsion. Cambridge university press.

Moriyama, F., 1979. On an approximate numerical method for estimating the performance of marine propellers. Pap. Ship Res. Inst. 16 (6), 361–376.

OpenFOAMFoundation, 2019. OpenFOAM version 7. URL https://openfoam.org/download/7-source/.

Phillips, A.B., Turnock, S.R., Furlong, M., 2009. Evaluation of manoeuvring coefficients of a self-propelled ship using a blade element momentum propeller model coupled to a Reynolds averaged Navier Stokes flow solver. Ocean Eng. 36 (15–16), 1217–1225.

Qiu, Y., Liu, Z., Chen, X., Zhan, C., 2010. Numerical calculation of maneuvering hydro-dynamic forces of drift ship based on SST turbulence model. In: 2nd International Conference on Computer Engineering and Technology, Chengdu, China.

Sanada, Y., Park, S., Kim, D.H., Wang, Z., Stern, F., Yasukawa, H., 2021. Experimental and computational study of hull–propeller–rudder interaction for steady turning circles. Phys. Fluids 33 (12), 127117.

Stern, F., Wilson, R.V., Coleman, H.W., Paterson, E.G., 2001. Comprehensive approach to verification and validation of CFD simulations—Part 1: methodology and procedures. J. Fluids Eng. 123 (4), 793–802.

Sumislawski, P., Sahab, A., Shevchuk, I., 2022. Numerical investigation of the JBC hull and propeller interaction under static drift condition. In: 34th Symposium on Naval Hydrodynamics, Washington, United States, 26th June - 01 July 2022.

Turnock, S.R., Phillips, A.B., Furlong, M., 2008. Urans simulations of static draft and dynamic maneuvers of the KVLCC2 tanker. In: Workshop on Verification and Validation of Ship Maneuvering Simulation Methods-SIMMAN 2008. Force Technology, Copenhagen, Denmark.

Windén, B., 2014. Powering Performance of a Self Propelled Ship in Waves (Ph.D. thesis). University of Southampton, URL https://eprints.soton.ac.uk/390102/.

Windén, B., 2021a. An open-source framework for ship performance CFD. http://dx.doi.org/10.5957/tos-2021-22.

Windén, B., 2021b. Predicting the powering performance of different vessel types using an open-source CFD propulsion framework. In: SNAME Maritime Convention 2021, SMC 2021. http://dx.doi.org/10.5957/SMC-2021-132.

Yamazaki, R., 1968. On the propulsion theory of ships on still water-introduction. Mem. Faculty Eng., Kyushu Univ. 27 (4).

Yamazaki, R., 1998. Deduction of the simplified propeller theory. Trans.-West Japan Soc. Nav. Archit. 251–272.

Zhang, Y., 2023. Influence of Drift Angle on the Self-Propelled Ship's Powering Performance in Waves (Ph.D. thesis). University of Southampton, URL https://eprints.soton.ac.uk/483454/.

Zhang, Y., Hudson, D., Windén, B., Turnock, S., 2021. Evaluating the effects of drift angle on the self-propelled ship using blade element momentum theory. In: 23rd Numerical Towing Tank Symposium. Mülheim an der Ruhr, Germany.

Zhang, Y., Windén, B., Hudson, D., Turnock, S., 2022. Hydrodynamic performance of a self-propelled KCS at angle of drift including rudder forces. In: 24th Numerical Towing Tank Symposium. NUTTS Committee, Zagreb Croatia, 16 – 18 October 2022.